Characterization of Surface Ligands on Functionalized Magnetic Nanoparticles

Thesis submitted to the Faculty of Physics
of the University of Duisburg-Essen
in partial fulfillment of the requirement for the degree of
Master of Science
2016

Submitted by

Sabrina Masur
from Erkrath

Duisburg, February 2016

Advisory committee:

Prof. Dr. rer. nat. Michael Farle
Prof. Dr. rer. nat. Michael Winklhofer

Abstract

The synthesis of colloidal nanoparticles involves surfactant molecules which bind to the particle surface and stabilize nanoparticles against aggregation. Based on its covalent-bonding interaction with most metal surfaces, oleic acid is often used as a ligand system for various nanoparticle systems. Importantly, protecting molecule shells can also be used for further functionalization.

This thesis reports the experimental details for the preparation of monodisperse oleic acid coated magnetic iron oxide nanoparticles by a thermal decomposition method. The obtained nanoparticles were characterized by high-resolution transmission electron microscopy (HRTEM) and selected area electron diffraction (SAED) measurements. The coupling mechanism between molecule and metal surface was characterized using Fourier transform infrared spectroscopy (FTIR), which revealed a bridging bidentate coupling of the carboxylate to the nanoparticle surface. The magnetic properties of the particles were investigated using ferromagnetic (FMR) and electron paramagnetic resonance (EPR) absorption spectroscopy. Those measurements showed two specific EPR signals, originating directly from the metal-organic interface and the molecule's carbon chain.

Moreover, this thesis shows that the EPR signals due to the oleic acid ligand molecule can be used as a local probe. As part of this we investigated the temperature dependent shift of the resonance field position of the EPR spectra, which can be used to measure the exact temperature on the nanoparticle interface. Additionally, we also measured an angular dependent change in EPR resonance field, resulting from the stray field of cubic iron/iron oxide nanoparticles, which are in good agreement with micro magnetic simulations.

Kurzfassung

Zur Synthese von kolloidalen Nanopartikeln werden im allemeinen Tensidmoleküle verwendet, welche an die Partikeloberfläche binden und die Nanopartikel stabilisieren und vor Agglometarion schützen.

Bedingt duch die kovalente Bindung zwischen Ölsäure und den meisten Metalloberflächen, wird diese oft als Ligandensystem für die Synthese unterschiedlichster Nanopartikelsysteme verwendet. In einigen Fällen kann diese Molekül-Hülle auch zur weiteren Funktionalisierung der Partikel genutz werden.

Diese Arbeit zeigt unter anderem über die Herstellung monodisperser mit Ölsäure beschichteter Eisenoxid Nanopartikel mittels thermischer Zersetzungs Methode. Die so synthetisierten Nanopartikel wurden durch Transmissionselektronenmikroskopie (TEM), Rasterelektronenmikroskopie (SEM), ferromagnetischer Resonanz(FMR) und Elektronenspinresonanz (ESR) Messungen charakterisiert. Der Kopplungsmechanismus zwischen den Molekülen und der Metalloberfläche wurde mittels Fouriertransmormations Infrarot Spektroskopie (FTIR) bestimmt. Aufgrund der bidentat verbrückenden Kopplung zwischen dem Carboxylat und der Oberfläche der Nanopartikel entstehten zwei Elektronenspinresonanz Signale, welche direkt von der Metall-Molekül-Schnittstelle und aus der Kohlenstoffkette des Moleküls stammen.

Des Weiten zeigt diese Arbeit, dass die EPR-Signale der Ölsäure-Moleküle als lokale Sonde verwendet werden können. Im Zuge dessen wurde die temperaturabhängige Verschiebung der Resonanzfeldposition der EPR-Spektren untersucht. Diese kann verwendet werden, um die genaue Temperatur an der Nanopartikeloberfläche zu messen. Darüber hinaus wird gezeigt, dass eine streufeldabhängige Änderung in dem EPR-Resonanzfeldes für kubische Eisen / Eisenoxid-Nanopartikel existiert. Diese Messungen zeigen eine gute Übereinstimmung mit dem durch mikromagnetischen Simulationen berechneten Streufeld. Diese Messungen belegen, dass sich die Moleküle als Streufeld-Sonden eignen.

Aufgabenstellung der Masterarbeit

für Sabrina Masur

gestellt von: Prof. Dr. rer. nat. Michael Farle

Thema: Characterization of surface ligands on functionalized magnetic nanoparticles (Characterisierug des Ligandensystems an der Oberfläche von funktionalisierten Nanopartikeln)

Aufgabenstellung:

Im Rahmen der Masterarbeit werden funktionalisierte Eisen-Eisenoxid core-shell Nanopartikel (NP) mittels magnetischer Resonanz Messungen untersucht. Zur Funktionalisierung der NP werden Carbonsäure Moleküle wie zum Beispiel Ölsäure verwendet.

Aufgabe der Arbeit:

- Funktionalisierung der NP durch Carbonsäure
- Charakterisierung der Partikel-Morphologie und Kristallstruktur mittels Transmissionelektronmikroskopie (TEM)
- Untersuchung der Kopplung zwischen Molekül und Partikeloberfläche durch Fourier-Transformations Infrarot Spektroskopie (FTIR)
- Unterschiedliche Elektronenspinresonanz (ESR) Messungen zur Untersuchung der Einsatzmöglichkeiten der funktionalisierten NP z.B.
    - Temperaturabhängigkeit der ESR
    - Winkelabhängigkeit der ESR
    - Leistungsabhängigkeit der ESR

Contents

Abbreviations

ac	Alternating Current
AES	Auger Electron Spectroscopy
AFC	Automatic Frequency Control
arb. u.	arbitrary units
CA	Caprylic Acid
Cu	Copper
CVS	Chemical Vapour Synthesis
CW	Continuous Wave
EPR	Electron Paramagnetic Resonance
fcc	Face Centered Cubic
Fe	Iron
FMR	Ferromagnetic Resonance
FT	Fourier Transform
FTIR	Fourier Transform Infrared (Spectroscopy)
GaAs	Gallium-Arsenide
HRTEM	High Resolution Transmission Electron Microscope
ip	In-Plane
IR	Infrared
LLG	Landau-Lifschitz-Gilbert (equation)
NP	Nanoparticle
O	Oxygen
OA	Oleic Acid
oop	Out-Of-Plane
SAED	Selected Area Electron Diffraction
SEM	Scanning Electron Microscope
TE	Transversal Electric
TM	Transversal Magnetic
UHV	Ultra-High-Vacuum

Symbols

α - Gilbert damping

α_i - directional cosine

B_{res} - resonance field

$\vec{B}_{eff}$ - effective magnetic field

$\vec{B}_{ext}$ - external magnetic field

b_{rf} - perpendicular high frequency field component

χ''_{xx} - high frequency susceptibility

E_{kin} - kinetic energy

ΔE_{zeeman} - Zeeman energy splitting

$F_{crystal}$ - crystalline anisotropy energy

E_d - demagnetization energy

F_{cub} - cubic anisotropy

F_{zeeman} - Zeeman Energy

$F_{crystal}$ - crystalline anisotropy

F_{shape} - shape anisotropy

$F_{surface}$ - surface anisotropy

f - frequency

g - g tensor

γ - gyromagnetic ratio

$\hbar$ - reduced Planck's constant

$\vec{H}_d$ - demagnetization field

K_4 - fourth-order anisotropy constant

K_6- sixth-order anisotropy constant

λ - wavelength

$\vec{l}$ - angular momentum

$\vec{M}$ - magnetization

$\vec{\mu}$ - magnetic moment

μ_B - Bohr's magneton

μ_s - spin magnetic moment

$\underline{\underline{N}}$ - demagnetization tensor

ω - angular frequency ($2\pi f$)

P - power

$\vec{S}$ - spin vector

Note: Even though the magnetic flux density B has dimensions and units different from those of the magnetic field H. In this work, the term 'magnetic field' shall be used for the quantity B, which has the unit of tesla ($T = Vs/m^2$) as this nomenclature is of almost universal usage in magnetic resonance.

1 Introduction

Over the last years nanoscience, nanotechnology and nanomaterials have become an important field of scientific and technical research. Especially the interest in magnetic nanostructures [Kod99] and their technical applications as e.g. contrast agents for MRI [Pat08], catalysts [Lin13] and super-capacitors [Du09] has been increasing. Furthermore, based on their unique physical, chemical, thermal, and mechanical properties, magnetic nanoparticles offer a high potential for several biomedical applications, such as cellular therapy and as a tool for cell-biology research [Mah13]. Here those particles can be used for example as magnetic field-guided carriers for localizing drugs or for tumor hyperthermia [Lee15]. Therefore, a special surface coating of the magnetic particles is required, which has to be not only non-toxic and biocompatible but also allows for a targeted delivery with particle localization in a specific area. Thus, those magnetic nanoparticles ought to bind to drugs, proteins, enzymes or antibodies and can be directed to an organ or tumor using an external magnetic field gradient or can be heated in an alternating magnetic field for use in hyperthermia [Pan03, Dor12]. In addition, there has been an increasing interest in magnetoelectronic or spintronic devices, which integrate the use of both the charge and the spin of the electron [Ž04]. These devises are expected to provide functionalities for energy efficient spin-based recording and information processing. For these devices, it is e.g. desirable to establish a means to detect the resulting spin current. Recent results showed the possible use of surface coating molecules to detect the spin current of a ferromagnetic martial [Mar16b].

In this work, monodisperse $\mathrm{Fe_xO_y}$ nanoparticles were synthesized by thermal decomposition as described in literature [Kim07]. In this process, oleic acid molecules were used as a surfactant that both covers the growing particle and controls their size and morphology. The organic shell also controls the spacing and the coupling between particles when they are assembled on a substrate or in fluids. Because the magnetic structure and chemical composition of the surface layer usually is very different from the core of the nanoparticle, the interaction between the stabilizing ligand and the nanoparticle is critical and essential for both synthesis and application.

Therefore, this thesis discuss the chemical structure of the surfactant adsorbed on the iron oxide nanoparticle, and suggests a bonding model for the adsorbed molecule. The monodisperse single crystalline iron oxide core/shell nanoparticles will be investigated and characterized by transmission electron microscopy (TEM), scanning electron microscopy (SEM), ferro- (FMR) and electron paramagnetic resonance (EPR). Furthermore, Fourier transform infrared spectroscopy (FTIR) measurements will be used to confirm the presence of the functional groups on the particle surface and to characterize the molecular coupling mode. The FMR and EPR measurements will be conducted to analyse the oleic acid molecules ability to generate EPR centres and act as a surface sensitive EPR probe. In order to investigate the origin of those EPR signals, several experiments on different nanoparticle systems and with different carboxylic acid molecules will be discussed. Moreover, in-situ measurements under ultra-high vacuum conditions will be shown to evaluate the role of the oxide shell for the paramagnetic resonance signals.

In addition, this thesis will demonstrate two possible applications for the molecule as a surface sensitive paramagnetic probe. As mentioned before, for biomedical applications temperature measurements with high spatial resolution and accuracy are an active area of research. Here, Riedinger et al. had reported a molecular temperature probe based on the thermal decomposition of a thermo-sensitive molecule to measure the temperature profile at the nanoparticle surface with a subnanometer resolution [Rie13]. However, this attempt toward temperature mapping has the disadvantage that the thermo-labile ligands are anchored to the superparamagnetic particles via PEG spacers. Thus they are not directly coupled to the particle surface. In this work, temperature dependent FMR and EPR measurements are conducted to characterize the oleic acid molecule's ability to act as a temperature probe directly at the particle surface.

Moreover, literature shows the possibility of EPR centres to map the strayfield of magnetic nanoparticles [Rak04, Sch81]. Here, Moore and Rodbell demonstrated the mapping of demagnetization fields at the surface of the coin-shaped sample by measuring the shift in the resonance field of a small chip of the free radical DPPH in intimate contact with the sample surface [Moo64]. In the context of this work, angular dependent measurements will be analysed to test the molecule's EPR centres possible use as stray field detector. Therefore this approach yields the advantage to characterize the stray field without attaching molecular radicals such as DPPH, but use the already functionalized molecule shell as a magnetisation monitor. For further validation, micromagnetic simulations of cubic iron/iron oxide nanoparticles will be shown and discussed in connection with the measurements.

The thesis is structured as follows:

Subsequent to the introduction in Chapter 1 the relevant physical fundamentals in the context of this work are summarized: In Chapter 2, carboxylic molecules are introduced and their chemical properties are briefly summarized. Here the main focus is the molecules coupling mechanism and their oxidation. Chapter 3 includes discussions on the theoretical background of the electron paramagnetic and ferromagnetic resonance effects. Moreover, the magnetic anisotropies of monodisperse magnetic nanoparticles are introduced, which are required for the correct interpretation of the results in Chapter 7.2. The experimental techniques which were utilized for structural and magnetic characterization are presented in Chapter 4. In Chapter 5 the different synthesis routes of the iron oxide nanoparticles and the TiO_2 preparation are explained and the particle are characterised in detail. The first results regarding the EPR signals, which arise from the molecule are discussed in Chapter 6. Here, a detailed investigation of the molecules' EPR signal is given by analysing several experiments with different nanoparticle systems and acids. Additionally, information of the molecules coupling mechanism and measurements with different carboxylic acids are illustrated. The experimental results on the EPR's origins are briefly summarized in Section 6.5. In Chapter 7 two possible applications as a surface-sensitive probe are discussed: It is demonstrated how the surface temperature of nanoparticles can be determined by using the resonance field of the EPR centre in the carboxylic molecule attached to the particle's surface as a temperature monitor. Furthermore, angular dependent measurements on different nanoparticle configurations are presented. For a better understanding of this behaviour, micromagnetic simulations have been performed and are discussed in Section 7.2.1. Chapter 8 provides the conclusion.

2 Structure and physical properties of the surfactant molecules

This chapter gives an introduction to the theory and functionality of carboxylic acid molecules. Since the main focus of this work is the analysis of the molecule and its ability to act as a surface sensitive sensor, a detailed understanding of the molecules coupling mechanism and chemical characteristics is required for the quantitative interpretations of the main results. More detailed information on carboxylic acids can be found in references [Tho00] and [Fra07].

2.1 Description of the molecular structure of carboxylic acids

Carboxylic acids are hydrocarbon molecules, containing a carboxylic (COOH) functional head group (Figure 2.1(a)). In this functional group, a carbon forms a double bond to one oxygen atom, called a carbonyl moiety (C=O), which in return is bonded to a hydroxyl group (OH), as seen in Figure 2.1(b). The combination of those two moieties results in the molecules chemical properties, the most notable of which is it's acidity.

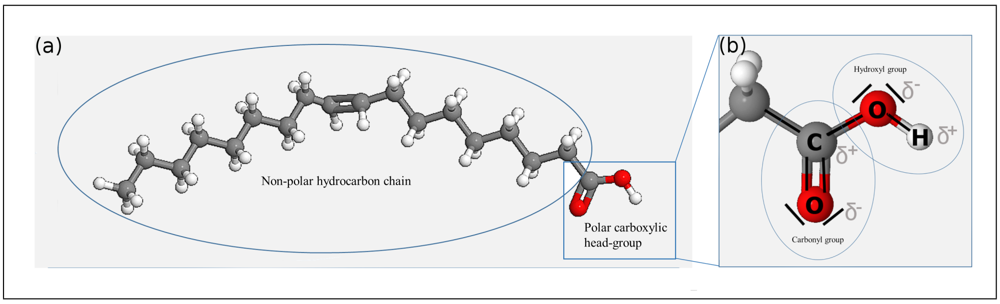

Figure 2.1: *Ball-and-stick model of an oleic acid molecule with the apolar hydrocarbon chain and the polar carboxyl head group (a) and the charge of the hydroxyl and carbonyl moieties (b). In this sketch, the grey atoms represent carbon, the white ones hydrogen and the red ones oxygen.*

$$\mathrm{RCOOH} \rightleftharpoons \mathrm{RCOO}^- + \mathrm{H}^+ \tag{2.1.1}$$

This acidity arises mostly due to the organic functional group's high polarity [Fra07]. If oxygen, as a electronegative atom, is covalently bound to carbon or hydrogen, a strong permanent dipole is formed, which makes the functional group hydrophilic, as illustrated in Figure 2.1(b). The hydrocarbon chain on the other hand is non-polar and thus is hydrophobic. Therefore carboxylic acid molecules are amphiphilic compounds, possessing both hydrophilic (polar) and hydrophobic (non-polar) properties.

As described in more detail in Chapter 5.1.1, oleic acid is used as the organic surfactant molecule. The molecule's hydrophobic carbon chain stabilizes the particles and prevents them from agglomeration [Kim07]. Furthermore, the chain extends to the solvent and thus determines the particles solubility and provides a hydrophobic surface. The hydrophilic head group on the other hand couples to the particle surface and hence prevents the particle from further growth. The selective adsorption of the oleic acid molecules on different crystallographic surfaces of the nanoparticles also directs the morphology, resulting e.g. in the cubic-shaped particles with six {001} surface facets used in this thesis. Due to this properties, oleic acid is one of the surfactants most commonly used to control the shape, size and aspect ratio of different nanostructures during synthesis [Wu08, Vo09].

2.2 Surfactant molecules and their different coupling mechanisms

As mentioned before, the synthesis of nanoparticles requires not only a amphiphilic ligand system, but the molecules should also be able to couple to the nanoparticle surface to control the morphology and size distribution. Therefore it is essential to understand the molecules functional head group and it's ability to couple to a metal surface.

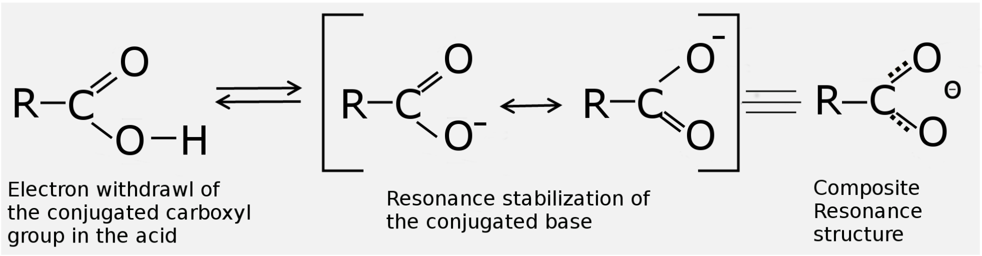

Figure 2.2: Sketch of the resonance stabilization of the conjugate base for carboxylic acid molecules. This stabilisations results in the formation of a carboxylate ion with a delocalized electron (indicated by the dotted line). In this sketch C represents carbon atoms, O oxygen atoms and R is any carbon chain attached to the carboxylic head group.

The molecules carbonyl group has an electron deficient carbon atom due to π-bonding (double bond) to an electronegative oxygen. In addition, this carbonyl carbon is also directly linked to a second electronegative oxygen atom bearing a hydrogen atom (Figure 2.1(b)). The ability of carboxylic acids to ionize and behave as acids is a direct function of the electronic properties and bonding order of these atoms. This electronic arrangement allows for the loss of a proton and ionization because the electron density is pulled away from the hydroxyl hydrogen through the conjugated carboxyl group. The charge formed upon ionization is stabilized by resonance delocalization, as depicted in Figure 2.2. Thus this resonance allows the negative charge to be delocalized between the two electronegative oxygen atoms (indicted by the dotted line in Figure 2.2). The so formed conjugated base of a carboxylic acid is called carboxylate ion. This ion can couple to the surface of a nanoparticle because the metal coordination group of the molecule is typically an electron donator and thus allows the coupling to the electron-poor metal surface atoms [Yin05].

The carboxylate ion can coordinate to metals in a number of different ways, e.g. in a unidentate, a chelating or in a bridging bidentate configuration. Examples of the arrangements are given with the Figure 2.3(a-c). Previous studies by Deacon et al. [Dea80] indicated, that the type of interaction between the carboxylate head and metal atoms can be identified using Fourier transform infrared (FTIR) spectroscopy. Here, the coupling can be categorized by the wavenumber separation Δ, between the asymmetric ν_{as}(COO-) and symmetric ν_s(COO-) stretch vibrations into the three types (see Chapter 6.1):

- Δ $(200 - 320\,\mathrm{cm}^{-1})$ monodentate,
- Δ $(140 - 190\,\mathrm{cm}^{-1})$ bridging bidentate,
- Δ $(< 110\,\mathrm{cm}^{-1})$ chelating bidentate,

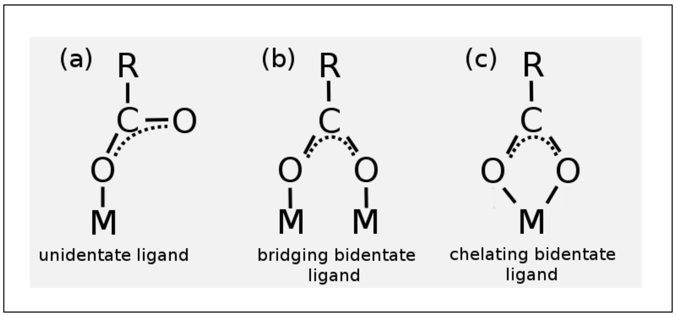

Figure 2.3: *The carboxylate ion can coordinate to a metal surface in a unidentate (a), a chelating (b) or in a bridging bidentate (c) configuration. In this sketch M represents a metal atom, C carbon, O oxygen and R is any carbon chain attached to the carboxyl head group.*

2.3 Oxdidation of fatty acids

A carboxylic acid with a long aliphatic chain is also called a fatty acid, which is defined by the number and conformation of carbon double bonds in their chemical structure. Thus, a hydrocarbon molecule containing no double bonds is called a saturated fatty acid because all carbon atoms are completely "saturated" with hydrogen atoms, whereas a molecule containing a double bond is called unsaturated [Gun96]. This chemical composition defines fatty acids within their various functional properties, wherein the difference in oxidation is the most important one in this thesis.

The most important lipids involved in oxidation are the unsaturated fatty acid moeties like oleic (one double bond), linoleic (two double bonds), and linolenic (three double bond) acid, but the following discussion will mainly focus on oleic acid molecules due to their importance for this thesis.

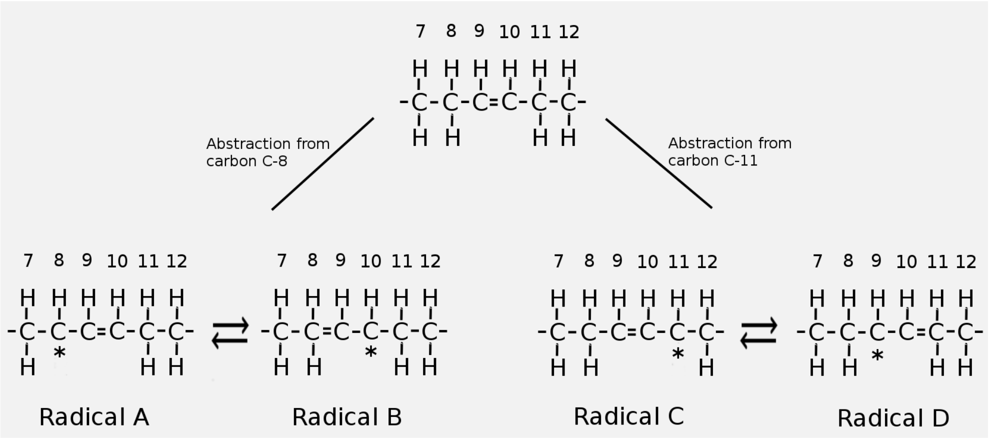

Figure 2.4: In case of oxidation of fatty acids, a hydrogen atom can be removed from the carbon atoms adjacent to the double bond. The loss of hxdrogen from carbon 8 results in two radicals A and B which are positional isomers of each other stabilized by resonance. Or a hydrogen loss from C11 could occur, resulting in the two radicals C and D.

For this molecule a hydrogen atom can be removed from either carbon C-8 or C-10, as these positions are located adjacent to the double bond, as illustrated in Figure 2.4. The loss of hydrogen from carbon C-8 results in two radicals A and B, which are positional isomers of each other stabilized by resonance. Or hydrogen loss from carbon C-11 could occur, resulting in the two radicals C and D. In either case, a free radical is formed by removing the labile hydrogen from the carbon atom, which can be detected by electron paramagnetic resonance (Chapter 6).

Literature also shows, that the oxidation of unsaturated fatty acids normally proceeds quite slowly but can be greatly stimulated by the presence of iron oxides and iron salts [Bra87]. This increased oxidation rate is mainly due to an enhancement of the initiation reactions as well as due to iron catalysis of lipid hydroperoxide decomposition reactions [Ern82].

In this thesis two different carboxylic acid molecules are used:

- Oleic acid ($C_{18}H_{34}O_2$) is an unsaturated fatty acid, which is commercially used in the preparation of oleates, lotions, and as a pharmaceutical solvent [Tho00]. It has a molecular weight of 282.4 g/mo and on exposure to air this molecule oxidises and acquires a brown color and rancid odor.

- Caprylic acid ($C_8H_{16}O_2$) is a saturated medium-chain fatty acid with a straight 8-carbon chain. Is is found naturally in milk, coconut oil and palm kernel oil [Tho00]. Unlike the previously described oleic acid molecule, caprylic acid does not have a carbon double bond, which means that caprylic acid oxidizes approximately 10 times slower, if at all.

3 Concepts in magnetism

The following chapter will give an overview of the basic magnetic effects, which are vital for the understanding and interpretation of the later presented results. They also build the basis for the measurement techniques in Chapter 4.1.

First of all, the microscopic behaviour of a paramagnet in an external magnetic field is described, to give the theoretical background on electron paramagnetic resonance. The here presented theory is freely reproduced after reference [Eat10, Wei07].

Next, to lay out the fundamental principles of the experimental technique of FMR employed in this thesis, an brief introductory descriptions of the ferromagnetic resonance effect is given. A more detailed description of the phenomena of FMR can be found in reference [Von66]. Thereafter, the magnetic anisotropies are introduced, which are the basis for Chapter 7.2.

It should be noted that it is not the goal of this thesis to give a complete mathematical description of these phenomena, and only those aspects will be addressed in more detail which are necessary for the general understanding of the results achieved within this work.

3.1 Electron paramagnetic resonance

Electron paramagnetic resonance, which is also called electron spin resonance is a physical effect, which is based on the absorption of electromagnetic radiation by a paramagnetic sample placed in a magnetic field. Here, the paramagnetic properties of the atoms are originating from uncompensated electron spins. Even though different spin states are possible, this introduction to EPR focuses primarily on molecules or atoms with a single free unpaired electron.

Electrons are usually characterized by both their charge and by an intrinsic mechanical angular momentum called spin. This momentum is a vector property that is defined by a magnitude and by a direction in space and is usually indicated by the spin vector $\vec{S}$. However, because an electron is a quantum particle, the behaviour of its spin is controlled by the rules of quantum mechanics, meaning that for a first approach to the magnetic resonance phenomenon, it is sufficient to know that the electron spin can be in two states, usually indicated by the Greek letters α (S=1/2) and β (S=-1/2). Those two states only differ in their orientation in space but not in their magnitude. By defining z as the quantisation axis of the system, the z-component of the spin vector

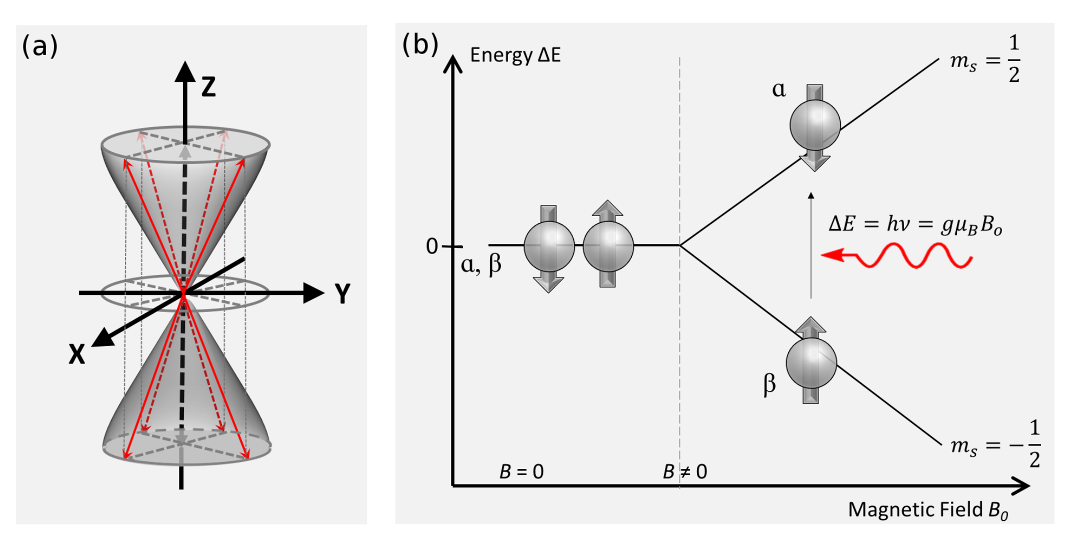

Figure 3.1: *(a) The electron spin angular momentum is represented in this Figure as a solid red vector. The z-component of the spin vector is shown as a dotted projection pointing in the positive or negative z direction. The xy-components in the plane perpendicular to z are not defined, thus the α and β spins could point in any direction on the surface of a cone. (b) At zero field ($B = 0$) the spin states α and β represented by up and down arrows are degenerated and have the same energy, which is zero in the energy scale. In the presence of a static magnetic field ($B \neq 0$) the α and β spin states split, which is called Zeeman splitting. This energy separation is proportional to the magnetic field intensity and the electron g-factor.*

can only point in the positive or negative z direction. The xy-components on the other hand are not defined, thus the α and β electron spin states could point in any direction on the surface of a cone. This effect is shown graphically in Figure 3.1(a). Figure 3.1(b) further shows, that as long as the space is isotropic (e.g. no external magnetic field) the α and β spin states have the same energy and are therefore degenerated.

Another particle property associated with the electron spin angular momentum $\vec{S}$ is the spin magnetic moment $\vec{\mu_s}$.

$$\vec{\mu_s} = g\mu_B\vec{S} \tag{3.1.1}$$

Here, g is the Landé factor or simply g-factor whereas μ_B is the atomic unit of the magnetic moment, which is called the Bohr magneton. If the electron is now exposed to a static magnetic field B_{ext} along the z-direction, this field will interact with the electrons magnetic moment in a way that the applied field splits the two spin states α and β. Since energy is quantized, the isolated electron spin has only two possible orientations along the z-direction in the external field, as mentioned before. Meaning, that it only has a state of lower energy when the moment of the electron is aligned parallel to the magnetic field (β-state) and a higher energy state when it is aligned anti-parallel (α-state), as illustrated in Figure 3.1(b). The splitting of these energy levels is called the Zeeman splitting, and the interaction of an electron magnetic moment with an external applied magnetic field is called the electron Zeeman interaction. The distance between those levels is a function of the magnetic field and can be described by the following equation

$$\Delta E = E_\alpha - E_\beta = h\nu = \hbar\omega = g\mu_B B_{ext} \tag{3.1.2}$$

A transitions between the two electronic Zeeman levels may be induced by an oscillating electromagnetic field b_{rf} if its energy matches the the energy difference ΔE between the α and β spin states. This effect is the fundamental basis for EPR spectroscopy.

In the case of not very weak magnetic fields and a definite frequency ω_0 for the high frequency field b_{rf} one can obtain the universal connexion between the resonant frequency and the external field from equation 3.1.2.

$$B_{res} = \frac{1}{\gamma}\omega_0 \tag{3.1.3}$$

where

$$\gamma = \frac{g\mu_B}{\hbar} \tag{3.1.4}$$

Here one has to note that Planck's universal quantum constant h is not present in equation 3.1.3. Therefore according to the principle of correspondence this equation can be obtained exactly within the framework of classical approximation and one can use this approach for atomic magnetic resonance, magnetic resonance phenomena in solids, and for the theoretical explanation of the laws of ferromagnetic resonance in particular [Von66].

Because equation 3.1.3 is classical in nature, an electron in a magnetic field can be represented by a spinning magnetic top. This motion of the magnetization $\vec{M}$ for non-interacting particles, whether induced simply by tilting the effective field away from the magnetization orientation or by resonant excitation of transitions in the Zeeman multiplets, can be described by the Landau-Lifschitz equation of motion [Lan35].

$$\frac{\partial \vec{M}}{\partial t} = -\gamma\left(\vec{M} \times \vec{B}_{ext}\right) \tag{3.1.5}$$

Here the cross product of M with $\vec{B}_{ext}$ describes a torque acting on the magnetization forcing it to precess around the effective field. For purely isotropic samples the motion is circular around $\vec{B}_{eff}$, but it becomes elliptic if the acting field is anisotropic.

3.2 Ferromagnetic resonance

The here presented basic theory of ferromagnetic resonance is freely reproduced after the book “Ferromagnetic Resonance” by S. V. Vonsovskii, thus for a more complete survey of the phenomenological theory one should consult reference [Von66].

Compared to a paramagnet, the resonance phenomena of a ferromagnet is not determined by individual isolated spins but by a complex system of strongly interacting electrons. Even without an external magnetic field this coupling between individual electrons in a single domain leads to uncompensated magnetic spin moments, which are all orientated parallel to each other. By applying an external magnetic field even a multi-domain sample can be homogeneously magnetized up to the total disappearance of the domain structure. In this case the magnetization vector $\vec{M}$, which is equal to the vector sum of the magnetic moments in a unit volume, is parallel to the external magnetic field. Therefore, the ferromagnet's individual moments can be described as a macro-spin, where an ensemble of spins can be considered as a total spin moment [Pol49]. Thus, in contrast to EPR, if an electromagnetic wave interacts with a ferromagnetic material, the spins are excited collectively (Magnon).

In the case of ferromagnetic materials, the various effect of the internal interactions lead to the need of a certain effective magnetic field B_{eff} in equation 3.1.5 instead of the external field B_{ext}. Thus the equation 3.1.5 becomes:

$$\frac{\partial \vec{M}}{\partial t} = -\gamma \left(\vec{M} \times \vec{B}_{eff} \right) \tag{3.2.1}$$

Here $\vec{B}_{eff}$ is the effective field consisting of the anisotropy fields and the external magnetic field. This equation (2.3) only describes the undamped free precession of the spin system's magnetization vector in a constant external field.

In a ferromagnet, this precession loses energy due to interactions in the spin system itself and by interactions between the spin system and its material surroundings [Von66]. Thus one has to take an additional relaxation term into consideration, describing the intrinsic damping. This damping mainly results from a transfer of energy from the precessing spin system to the lattice vibrations. One phenomenological description of the losses into the torque equation was introduced by T. L. Gilbert in 1955 [Gil04] and leads to following equation:

$$\frac{\partial \vec{M}}{\partial t} = -\gamma \left(\vec{M} \times \vec{B}_{eff} \right) + \frac{\eta}{M} \left(\vec{M} \times \frac{d\vec{M}}{dt} \right) \tag{3.2.2}$$

This equation is known as Landau-Lifschitz-Gilbert (LLG) equation containing the dimensionless damping parameter η, which is commonly substituted by

$$\eta = \frac{G}{\gamma \mu_0 M_s} \tag{3.2.3}$$

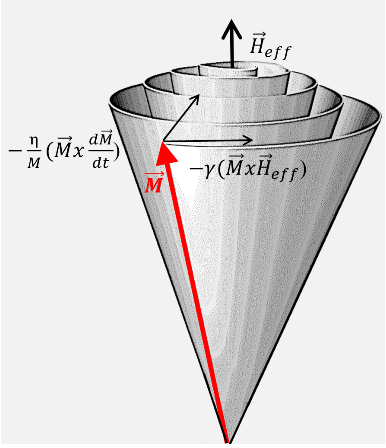

Figure 3.2: *Schematic of magnetisation dynamics. The magnetisation vector $\vec{M}$ (red arrow) precesses around the effective magnetic field $\vec{H}_{eff}$ (which has the same direction as B_{eff}) following the Landau-Lifschitz-Gilbert equation. The phenomenological damping term $\frac{\eta}{M}(\vec{M} \times d\vec{M}/dt)$, causes the magnetic motion to relax towards the direction of $\vec{H}_{eff}$. For a better visualization the opening angle $\measuredangle(\vec{M}, \vec{H}_{eff})$ is grossly exaggerated.*

to express damping in terms of relaxation rates using the Gilbert damping parameter G. This damping term causes the magnetic motion to relax back towards the direction of $\vec{B}_{eff}$. Figure 3.2 depicts the motion described by equation (3.2.2).

To understand the measurement principle, one has to consider the free energy density of the magnetization. Here, the following equations connect the the magnetization $\vec{M}$ which precesses in an external high frequency field around the effective magnetic field with free energy of the magnetization [Mec97]:

$$\vec{M} = \vec{M_s} + \vec{m}e^{iwt} \quad ; \vec{B_{eff}} = \begin{pmatrix} b_{rf}e^{i\omega t} \\ 0 \\ B_{ext} \end{pmatrix} + \begin{pmatrix} F_{M_x} \\ F_{M_y} \\ F_{M_z} \end{pmatrix} \quad ; F_{M_i} = \frac{\partial F}{\partial M_i} \tag{3.2.4}$$

Here, one can see that the effective magnetic field B_{eff} consists of the high frequency magnetic field component, the applied external field, and the field inside the sample, produced by the magnetic anisotropy (F_{M_i}, i= x, y, z). All the relevant anisotropy contributions are included in the free energy density:

$$F = F_{crystal} + F_{shape} + F_{surface} \tag{3.2.5}$$

The absorption signal of ferromagnetic resonance is proportional to the imaginary part of the high frequency susceptibility tensor χ'', as can be seen by solving equations 3.2.4 in the following form [Mec97]

$$\vec{m} = \overset{\leftrightarrow}{\chi} \vec{b_{rf}} \tag{3.2.6}$$

3.3 Magnetic anisotropies

The phenomenon of preferred orientations of the magnetization in ferromagnetic materials in the absence of an external magnetic field is called magnetic anisotropy. The origin of those preferred directions is mainly caused by two different mechanisms:

- spin-orbit coupling
- dipole-dipole interaction

In the following sections the causes of magneto-crystalline, shape and surface anisotropy are explained in more detail, which make up the major contribution in the magnetic anisotropy for the iron films and magnetic iron oxide nanoparticles investigated within the framework of this thesis. The understanding of those anisotropies are vital for the correct interpretation of the later presented results of the angular dependent FMR and EPR measurements in Chapter 7.2. Furthermore, a cubic magneto-crystalline anisotropy was taken into account for the later discussed micromagnetic simulations (Chapter 7.2).

The coordinate system used in this thesis to define the magnetisation's direction with respect to the sample geometry is shown in Figure 3.3. In the following, the angle $\theta_{\vec{M}}, \vec{B}_{ext}$ is the polar angle and $\phi_{\vec{M}}, \vec{B}_{ext}$ the azimuthal angle of the magnetization and the external magnetic field inclined with the sample coordinate system. The vector $\vec{B}_{ext}$ and $\vec{M}$ correspond to the magnetization and the external magnetic field.

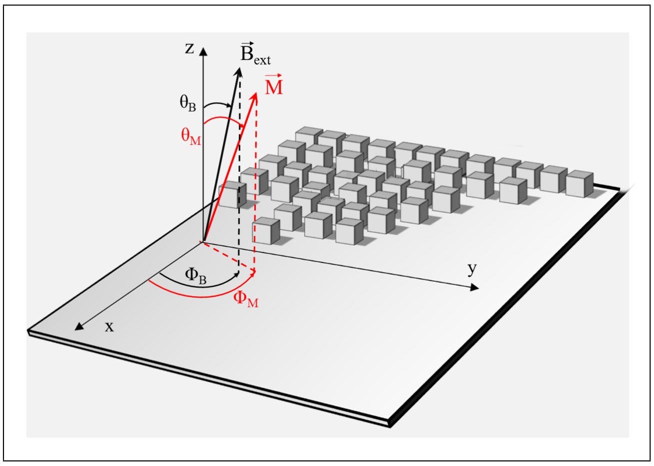

Figure 3.3: *The coordinate system used to define the magnetisation's direction with respect to the sample geometry. θ is the polar angle and ϕ the azimuthal angel of the magnetization inclined with the sample coordinate system. $\vec{B}_{ext}$ is the external magnetic field, and $\vec{M}$ is the magnetisation vector in the system. The cubes represent the measured iron oxide nanocubes, wich form an almost two dimensional layer (Chapter 7.2).*

3.3.1 Shape anisotropy

The shape of a ferromagnetic sample has great influence on the direction of the magnetization. This is normally due to long-range dipolar interactions between magnetic moments in the material. These dipolar interactions produce magnetic charges or poles at the surface, which are the source of the so called demagnetizing field ($\vec{H}_d$). This field normally dependence on the sample morphology, meaning that for non-spherical particle, the demagnetizing field will not be equal for all directions,

The magneto-static energy, which is the energy associated with the demagnetizing field of a homogeneously magnetised sample, can be expressed by the following equations:

$$E_d = -\frac{\mu_0}{2} \int \vec{M} \vec{H}_d \, dV \tag{3.3.1}$$

$\vec{H}_d$ is the internal demagnetisation field of a uniformly magnetized object and can be expressed in terms of the demagnetisation tensor $\overset{\leftrightarrow}{N}$,

$$\vec{H}_d = - \overset{\leftrightarrow}{N} \vec{M} \tag{3.3.2}$$

which will be isotropic for a spherical body, due to the rotational invariance, but becomes anisotropic for other shapes. A thin film for example can be considered as a 2-dimensional layer with infinite expansion in the x- and y-direction. This condition yields a demagnetisation tensor of $N_{11} = N_{22} = 0$ and $N_{33} = 1$ [Kit05], thus equation (3.3.1) becomes

$$F_{shape} = \frac{E_d}{V} = \frac{1}{2} \mu_0 M^2 \alpha_z^3 \tag{3.3.3}$$

with the direction cosines $\alpha_i = \frac{M_i}{M_s}$ (i = x, z, y) of the magnetization vector relative to the sample's principal axes, as indicated in Figure 3.3. Because the nanoparticle samples used in Chapter 7.2 form a close-packed layer, they can be considered as a thin film with a slight modification in formula (3.3.3) by the filling factor f

$$F_{shape} = \frac{1}{2} \mu_0 f M^2 \alpha_z^3 \tag{3.3.4}$$

This factor takes into account the difference in volume for a statistically distributed layer of separated nanoparticles compared to a continuous and closed layer [Spa02].

3.3.2 Magneto-crystalline anisotropy

For a ferromagnet with a crystalline structure like the here used nanoparticles, energetic minima and maxima are present due to lattice symmetries. The reason for this anisotropy is the spin-orbit coupling in the material, which couples the magnetization to the crystal lattice [Hub98]. The value of this magneto-crystalline anisotropy energy depends on the anisotropy of the orbital momentum $\Delta\mu_l$ and spin-orbit coupling constants ζ [vdL98] and can be described as

$$E_{crystal} = \alpha \frac{\zeta}{4\mu_B} \Delta\mu_l \tag{3.3.5}$$

The prefactor α depends on the electronic structure of the sample [Wil00]. In the case of a crystal with cubic symmetry the energy can be represented by an exponential series

$$F_{crystal} = K_0 + K_4(\alpha_1^2\alpha_2^2 + \alpha_2^2\alpha_3^2 + \alpha_3^2\alpha_1^2) + K_6\alpha_1^2\alpha_2^2\alpha_3^2 + ... \tag{3.3.6}$$

where α_i are the direction cosines of the magnetisation relative to the edges of the cube and K_i (i = 0, 4, 6) are anisotropy constants [Von66].

For the core/shell nanoparticles used in this thesis it is important to note that the hard and easy axis of pure iron and magnetite are reverse. Meaning, that the easy and hard axis for iron are (100) and (111), respectively (Figure 3.4(a)). Whereas magnetite's easy and hard axis are (111) and (100) (Figure 3.4(b)), which will become important for the interpretation of the angular dependence in Chapter 7.2.

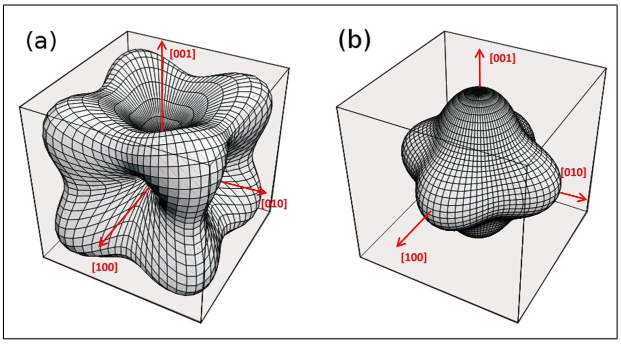

Figure 3.4: *A 3D-plot of the angular dependent magneto-crystalline anisotropy for a system with cubic symmetry and the anisotropy constant* $K_6 = 0$ *and (a)* $K_4<0$ *or (b)* $K_4>0$*, taken from [Ant07].*

3.3.3 Surface anisotropy

When working with nanoparticle, one has to consider the increasing surface to volume ratio. Therefore, in addition to the before mentioned magneto-crystalline and shape anisotropy, one has to take into account the surface anisotropy. This anisotropy arises due to the breaking of the local symmetry at the particle surface, which alters the electronic structure and magnetic interaction compared to the bulk properties and thus effects the orbital motion of electrons (spin-orbit coupling).

Figure 3.5 shows a truncated octahedron, which represents the nanoparticles used in this thesis. The surface of those particles consists of six {100} and eight {111} facets

[Jam04]. This holds true for the shape of both, the nanocubes described in Chapter 5.1.2 and the further oxidized nanoparticles described in Chapter 5.1.3, which have a more spherical shape.

The truncated octahedron is according to Wulff's theorem, the equilibrium shape of a fcc cluster [Jam04]. Consequently, the atoms at the edges, corners and plane facets vary in their coordination numbers and directions to their next neighbours [Jam04]. Besides the variation in surface anisotropies for different facets, additional step anisotropies might occur. Using N'éel's anisotropy model [Née54] the magnetic anisotropy is given by the sum of all the next neighbour's pair interactions $L(\vec{m}\vec{r_{ij}})^2$ and the surface anisotropy energy for the whole particle is given by:

$$E_{surf} = \frac{L}{2} \frac{\sum_{i,j} (\vec{m}\vec{r}_{ij})^2}{\|\vec{r}_{ij}\|^2} \tag{3.3.7}$$

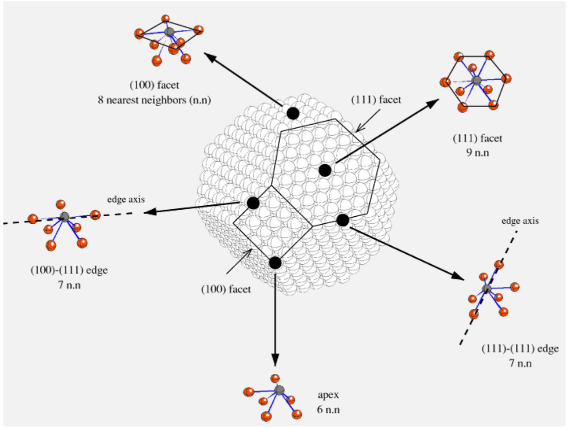

Figure 3.5: *The different atomic surface facets for a perfect truncated octahedron, which exhibits eight {111} and six {100} facets. The inlets represent the different surface atoms with their next neighbour configurations for the corresponding crystal facets. The octahedron contains 1289 atoms, adapted from [Jam04].*

4 Experimental methods

After the theoretical description of the phenomenon of ferro- and paramagentic resonance, the aim of this chapter is to provide basic information on the experimental methods and setups used in this thesis. Here, because the FMR and EPR measurements present the key results of this work, the magnetic resonance technique is described in more detail. Sample characterisation techniques, such as transmission electron microscopy, Auger electron spectroscopy and Fourier transform infrared spectroscopy are only briefly introduced.

4.1 Magnetic resonance technique

This section will cover the main components required for measuring both EPR and FMR experiments and their functional principle, freely reproduced after the books 'Electron Paramagnetic Resonance' from Bolton [Wei07] and 'Quantitative EPR' from Eaton [Eat10]. Thus, for more detailed information on the principal setup and all its components one should consult the previously mentioned references. In this thesis two different setups were used, one Elexsys spectrometer from Bruker and a modified Varian apparatus. The setups only slightly differ in their properties, but have the same measurement principal. Figure 4.1 shows the general layout of a typical EPR/FMR setup.

Microwave Bridge

The electromagnetic radiation source and the detector are situated in a microwave bridge (dotted line in Figure 4.1). Here, the microwave source is either a klystron (Varian setup) or in newer spectrometers a solid state source like a Gunn diode (Bruker Elexsys setup). The generated microwave enters a circulator, which guides the wave to the sample region by directing it from port 1 to the cavity (port 2). There it will be reflected back to the circulator, as will be described below. Because this device is non-reciprocal the measured microwave can not flow back to port 1 but only go to the detector through port 3. There a diode converts the incident microwave power through a resistor into a voltage, which is proportional to the reflected microwave power. During the measurement an automatic frequency control (AFC) is used to keep the setup tuned to the resonance frequency of the cavity. Therefore, the AFC "catches" the resonance dip of the resonator and keeps it critically coupled, regardless

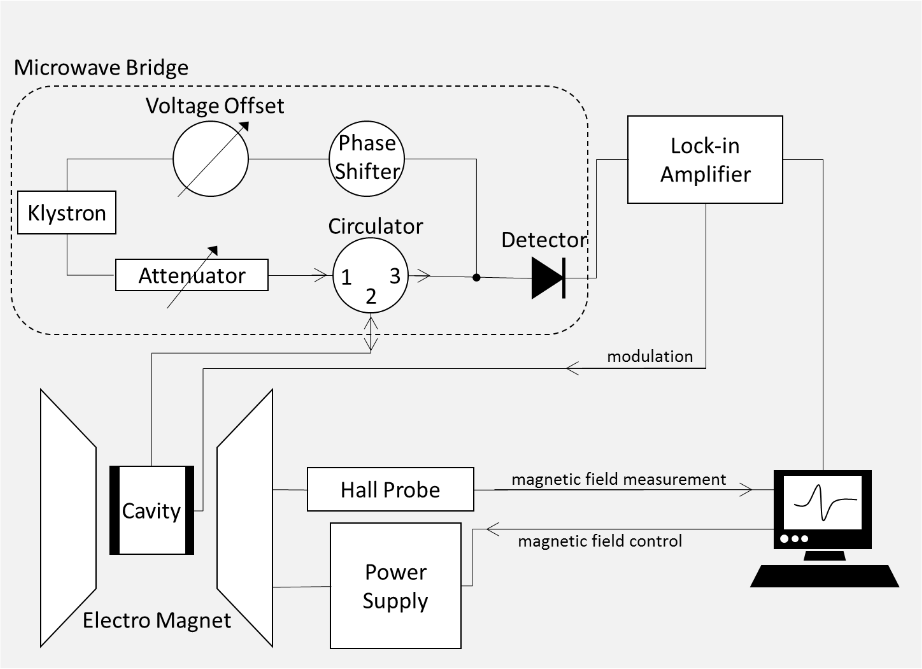

Figure 4.1: Schematic of a typical EPR and FMR setup with it major components: microwave bridge, cavity, electromagnet with powersupply and Lock-in amplifier.

of slight changes of the frequency during the measurement. Thus it improves the signal and the stability of the measurement. To insure that the diode operates as a linear detector[1] an additional reference arm is used, which supplies the detector with the required microwave power. After the combined signal is detected by the diode it is passed on to a lock-in amplifier to reduce noise and lastly to a computer, which is used for analysing the data as well as coordinating all the units for acquiring a spectrum.

Microwave Cavity

To amplify the weak signal, the sample is usually placed inside a resonator. In this thesis only classical hollow waveguide cavities are used. Here the frequency of the source is tuned to the corresponding resonant frequency of the cavity. By using an iris screw the microwave's phase is adjusted in a way that the microwave power remain inside the cavity and is not reflected back into the waveguide. This adjustment is called

---

[1] Diode current is proportional to the square root of the microwave power [Eat10]

critical coupling and can be achieved by matching the impedance of the waveguide to the cavity.

If both frequency and external field fulfill the samples resonance condition, it absorbs part of the microwave power, which in turn changes the impedance and quality factor of the cavity. Thus, the cavity is no longer critically coupled and microwave power is reflected back to the microwave bridge, resulting in an EPR/FMR signal. The power absorption from a unit volume of the sample is given by [Poo97]

$$P = \frac{1}{2\mu_0}\omega\chi'' \int_V b_{rf}^2 \, dV \tag{4.1.1}$$

For the angular dependent measurements conducted in this thesis (Chapter 7.2.1) one further has to consider the distribution of the magnetic and electric field of the standing wave inside the cavity before placing the sample. This is important, because most samples exhibit a non-resonant absorption of microwave power via the electric field, resulting in unwanted sample heating. Fortunately, the standing electromagnetic waves have their electric and magnetic field components exactly out of phase, which result in a spatial separation of the electric and magnetic fields in the cavity. The modes are referred to as transverse electric (TE) and transverse magnetic (TM).

Because the magnetic and electric field inside a cavity depend on the cavity's shape and dimensions, different cavities are optimised for different measurements. Thus two different cavities are used in this work. Firstly, a rectangular TE_{102} from Varian due to it's high flexibility for different applications and a cylindrical TE_{011} cavity ER 4119HS from Bruker, due to it's good resonance stability for angular dependent measurements. The subscripts designate the number of half-wavelengths along the according dimensions. The electric and magnetic field of both cavities are depicted in Figure 4.2. Both cavities work at a frequency of approximately 9.5 GHz.

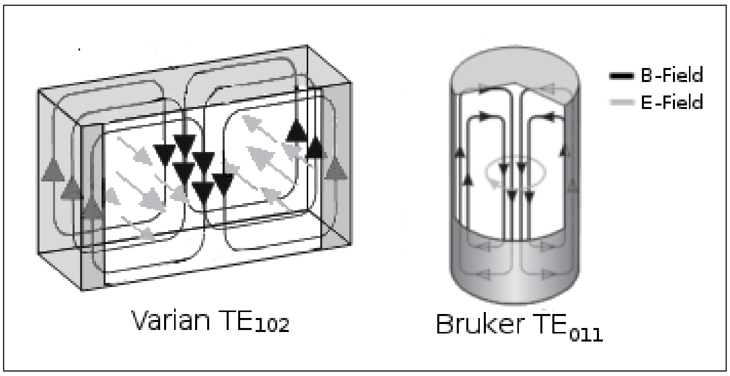

Figure 4.2: *Magnetic and electric field distribution in a Varian TE_{102} and a Bruker TE_{011} cavity. The black arrows represent the electric and the grey arrows represent the magnetic field. The two pictures are taken from reference [Eat10] and [Ant07].*

Magnetic Field and Lock-in Amplifier

In a typical fixed-frequency magnetic resonance spectrometer, the resonance condition is achieved by sweeping the external quasi-static magnetic field B_{ext}, which is commonly measured and controlled by a Hall-effect detector. This field should be stable and uniform over the whole sample volume.

To further increase the measurement's sensitivity an alternating high frequency field is superimposed on the static field. This is usually achieved by placing small Helmholtz coils on each side of the cavity along the axis of the external quasi-static field. Thus, the modulation field strength interacting with the sample is varied sinusoially at modulation frequencies from a few kHz to 100 kHz. Due to this modulation it is possible to use a phase-sensitive amplitude detection technique such as a lock-in amplifier. This technique allows to amplify the EPR signal and enhances the signal to noise ratio. It also results in the signal resembling the first derivative of an absorption line.

Additional Equipment

The temperature dependent EPR and FMR spectra in this thesis were recorded with a CW Bruker Elexsys E-500 spectrometer equipped with a Bruker Digital Temperature Control System ER 4131VT for liquid nitrogen cooling. Here, the sample is inserted into the quartz dewar, which is mounted to the cavity. The temperature was measured with a thermocouple close to the sample position and controlled using a digital flow control and temperature controller.

An ER 218PG1 programmable goniometer was used to measure the EPR spectra of the sample system as a function of their angular position with respect to the external applied magnetic field. One advantage of this goniometer is that it can be controlled by a computer, which in turn controls a stepper motor to position the sample with an angular resolution of 0.125 degree [Bru]. In this thesis, the goniometer was used to measure the angular dependence of the sample system. By choosing different sample holder rods, it was possible to rotate the samples both in-plane and out-of-plane, as seen in Chapter 7.2, Figure 7.4.

4.2 Additional experimental techniques

4.2.1 Vibrational spectroscopy

Vibrational Spectroscopy is an energy sensitive method, which is either based on periodic changes of dipolmoments (e.g. infrared spectroscopy) or polarizabilities caused by molecular vibrations (e.g. Raman spectroscopy). In this thesis, FTIR measurements were used to analyse the carboxylic acid molecule's coupling mechanism onto different sample systems. Furthermore, the Raman spectroscopy measurements were conducted to characterize the structural properties of the TiO_2 nanoparticles.

This chapter will only give a brief freely reproduced description of the basic principles taken from reference [Nak08a]. A more detailed descriptions on both measurement techniques can thus be found in this reference.

Fourier Transform Infrared Spectroscopy

Fourier transform infrared spectroscopy is a well established measurement technique to characterize molecular compositions of solids, liquids or gas. The approach is to transmit or reflect infrared (IR) light and observe the transmission or reflection profile, which occurs when the photon's electromagnetic field interacts with the molecular electric dipoles between vibrating atoms. Those dipoles are generally created due to unequal electro-negativities in the molecule's atoms. The frequency of this vibration is characteristic and unique for different functional groups relating to unique frequencies of light being absorbed.

The principal FTIR setup is based on a Michelson interferometer, which consists of an IR source, a beam splitter, a fixed mirror, a mirror that translates back and forth, and a detector as seen in Figure 4.3(a). IR radiation from the source is transmitted to the beam splitter, which splits the incident beam into two separate beams. Here one of them is reflected at a 90° angle onto a fixed mirror, while the other is transmitted to a flat mirror which moves back and forth at a constant velocity. The two beams are reflected from their respective mirrors and are recombined at the beam splitter. The

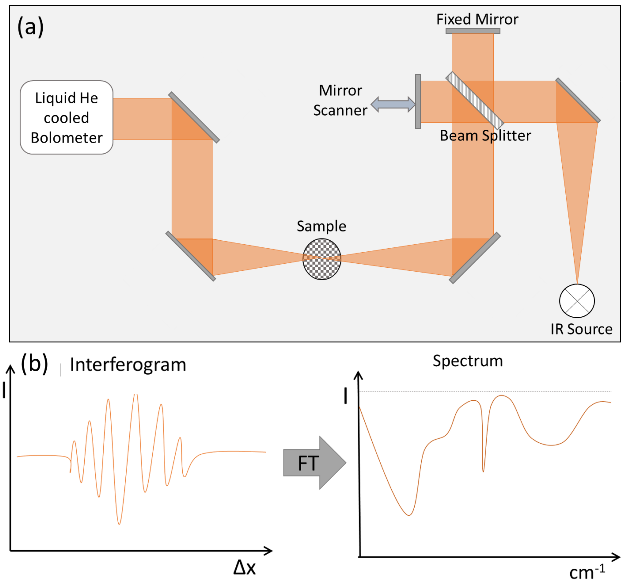

Figure 4.3: *(a) A schematic sketch of a typical Fourier transform infrared spectrometer and the associated beam path (in red). (b) A schematic sketch of how the high-spectral-content pulse is modified due to the sample and the subsequent Fourier transform to give a spectrum in frequency space.*

re-joined beam is then lead to the sample. The superposition of both beams, passing through the sample subsequently gives the measured interferogram. Performing a mathematical Fourier transform on this signal results in the spectrum, as shown in Figure 4.3(b).

Because the samples used in this thesis are either iron oxide nanoparticle or iron thin films, the samples were measured not in transmission but reflection. This reflectance techniques basically involve a mirror-like reflection from the sample surface and is used for samples such as iron thin films. The reflectance spectra differ from those recorded in transmission, as they appear as "derivative-like" bands. These spectra can be converted into absorption one by using of Kramers-Kronig transformation that is available in most spectrometer software packages. The spectrometer used in this thesis was a Bruker IFS 66v/S flexible vacuum FTIR spectrometer with a wavelength of 370-7500 cm^{-1}.

Raman Spectroscopy

The structural characterization of the TiO_2 nanoparticles was performed using a confocal Raman Spectrometer 'InVia' from Renishaw with a laser operating in a range from 532 nm to 633 nm.

To obtain a Raman spectrum, the sample is illuminated with a monochromatic light source (e.g. Laser). If the light hits the target, most of the light that scatters off is unchanged in energy, but a small fraction has either lost or gained energy because the photons exchange part of their energy with molecular vibrations in the material. This is called 'Raman scattering' and results in the distinctive Raman shift, which is the actual measurement signal. This technique is similar to the previously described infrared absorption spectroscopy, but has different selection rules.

4.2.2 Auger electron spectroscopy

In order to chemically characterize the oxidizing effect of oleic acid on pure iron films and the their state of oxidation, Auger electron spectroscopy (AES) measurements were performed using a Staib Instruments DESA 100 Auger spectrometer. The following depiction of this measurements technique is freely reproduced after reference [Lüt10]

The Auger effect is an electronic process resulting from the inter- and intrastate transitions of electrons in an excited atom due to impact ionization with an external electron beam or photon, which have energies in the range of several eV to 50 keV. If a photon hits a core state electron (e.g. K shell), it can be removed leaving behind a hole. As this is an unstable state, the core hole will be filled by an outer shell electron (e.g. L_1). Here the electron moving to the lower energy level loses an amount of energy equal to the difference in orbital energies. This energy can further couple to a second outer shell electron (e.g. $L_{2,3}$), which in turn will be emitted and ionizes the atom if the

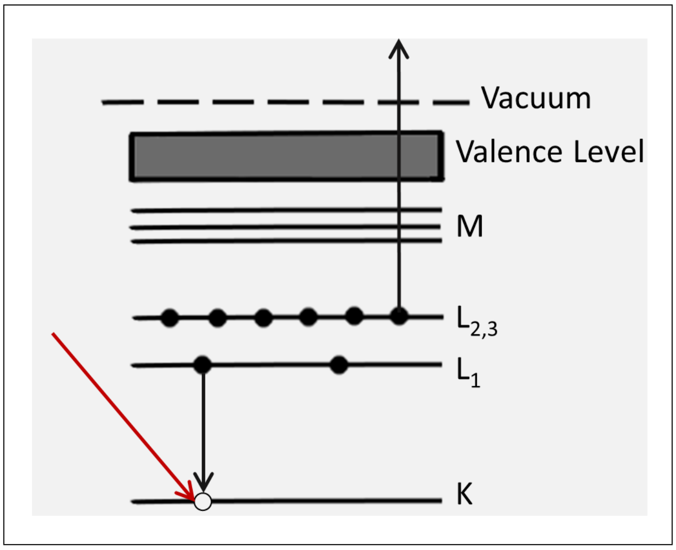

Figure 4.4: *Principle of Auger Electron Spectroscopy, in which the the primary hole is created via impact of an high energy electron or a photon, respectively. An electron from the L_1 level fills in the K-hole and the transition energy is imparted to a $L_{2,3}$ electron which is subsequently emitted. The Auger effect leaves the atom ionized.*

transferred energy is greater than the orbital binding energy. The process is shown in Figure 4.4. The emitted electron will thus have the element specific kinetic energy of:

$$E_{Kin} = (E_K - E_{L_1}) - E_{L_{2,3}} \tag{4.2.1}$$

In the experiment, a focused electron beam of approximately 0.5 mm with a kinetic energy of 3 keV to 7 keV is directed onto the sample and there triggers the Auger process. The emitted Auger electrons are detected and give a spectrum in which the number of detected electrons is applied over the kinetic energy. Because the mean free path of the used electron beam in the material in this energy range is low and the Auger electrons all have low-energy, electrons can only be emitted from a small sample depth of $0.2 - 3$ nm. Therefore, AES is a surface sensitive technique for the chemical characterization of e.g. thin films.

4.2.3 Transmission electron microscopy

High resolution transmission electron microscopy is an important structural characterization technique in materials science. In this thesis, it was used to get information on both structural and chemical properties of the iron oxide nanoparticles. All results reported herein were obtained on a Philips Tecnai F20 TEM/ STEM/ GIF Supertwin microscope (operating voltage 200 kV) with a field emission gun and a point resolution of 0.24 nm. A more detailed description of the TEM setup and it's functions can be found in reference [Els14], therefore this chapter will only give a brief description of the general operating principal.

The electrons are generated thermally at an electron gun and are then focused into an electron beam by different magnetic lenses. The beam is then transmitted through a thin sample and interacts with it. Subsequently, the focused electrons are scattered by the atomic columns, creating an image of the sample. The image is then enlarged by the intermediate and projector lenses onto a phosphorous screen, where the electrons produce light that can be recorded with standard camera techniques. The images will give information on the samples crystallinity and atomic distances. Figure 4.5 shows a simplified sketch of the TEM setup.

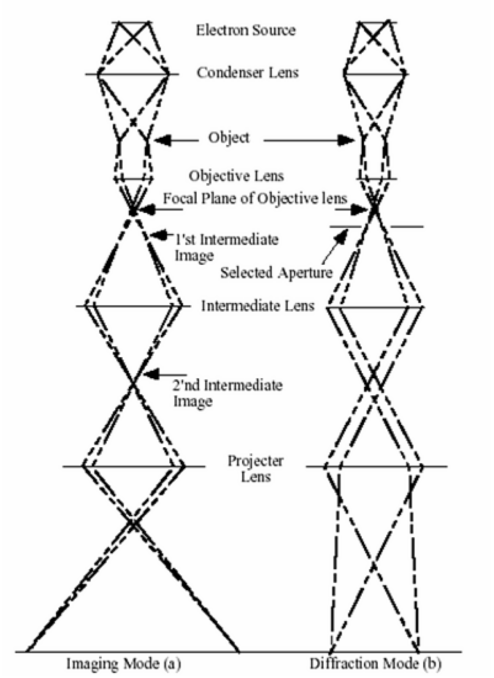

Figure 4.5: *Geometrical optics representation of the transmission electron microscope in imaging mode (a), and diffraction mode (b), adapted from reference [Kil].*

5 Sample preparation and characterization

The following chapter will give detailed information on the different material systems used in this thesis. Firstly, two iron nanoparticle systems are presented, which differ in their oxidation state, chemical composition and shape. Secondly, a short overview of the synthesis method and properties of the used TiO_2 nanoparticle is presented.

5.1 Iron nanoparticles

5.1.1 Synthesis

The iron/iron oxide nanoparticles were synthesized by thermal decomposition according to the procedure described by Hyeon [Kim07]. This method has the advantage of producing particles, which are well-controlled in size, shape and crystallinity. The here presented synthesis was done by Sara Liébana-Viñas from the workgroup of Michael Farle at the University Duisburg-Essen by the following procedure:

Iron (II) stearate (1.24 g, 2 mmol) and sodium oleate (0.1 g, 0.3 mmol) were dissolved in oleic acid (10 g) at room temperature. The mixture solution was degassed at 100 °C under argon atmosphere for 1 hour. After that, the mixture was heated to 380 °C with a heating rate of approximately 5 °C/min and the sample was kept at that temperature for one hour. The whole procedure was conducted under a continuous argon flow and vigorous magnetic stirring. After cooling down to room temperature, the sample was

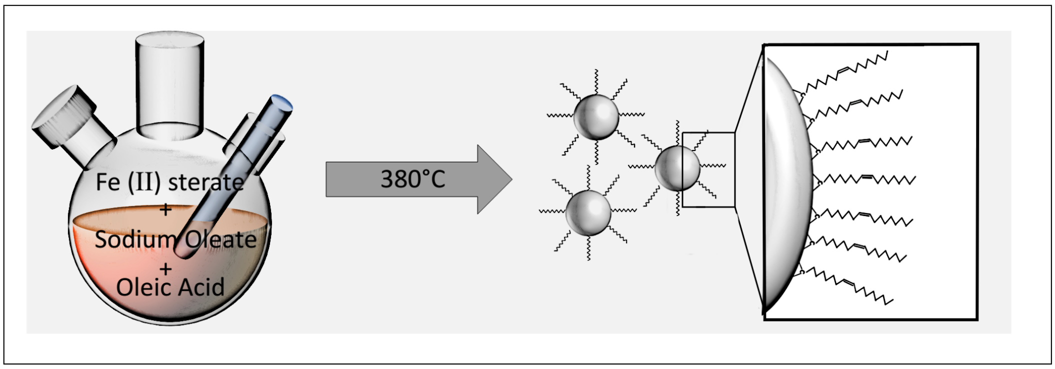

Figure 5.1: The thermal decomposition recipe for synthesizing Fe_xO_y nanoparticles capped with oleic acid molecules.

centrifuged and washed 4 times by sequential precipitation with a mixture of acetone, ethanol and hexane (5 : 1 : 1) to get rid of the unbound surfactant molecules. Finally, the particles were re-dispersed in n-hexane prior to deposition onto a substrate. A small sketch of the synthesis procedure is shown in Figure 5.1.

In this synthesis oleic acid is used as the organic surfactant molecule, because it controls the particle growth and prevents aggregation. Furthermore, the chain of the molecule extends to the solvent and thus determines the particle's solubility and provides a hydrophobic surface. The selective adsorption of the oleic acid molecules on different surface facets directs the morphology, resulting in e.g. cubic-shaped particles [Sha07].

5.1.2 Fe/Fe_xO_y nanocubes

Figure 5.2(a) shows a low-magnification bright-field TEM image of the nanoparticles on the amorphous carbon grid, which tend to self-assemble into a two-dimensional layer. Thereby, the inter-particle separation is approximately commensurate with two interdigitated layers of surfactant molecules, resulting in a side-by-side distance of 2.3 nm. Further analysis of the nanoparticles size distribution and aspect ratio with the program 'Digital Micrograph^{TM}' showed, that the vast majority of the particles have a cubic morphology (Figure 5.2(c)) with an average edge length of about 28.4 ± 1.7 nm (Figure 5.2(b)). This morphology, as already mentioned in Chapter 2, is caused by

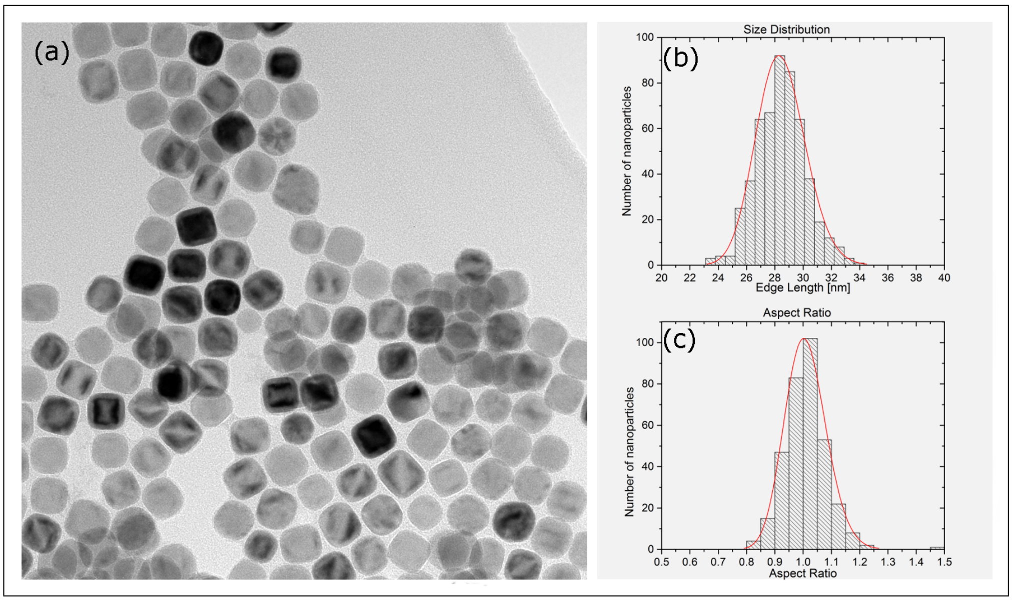

Figure 5.2: *Bright-field TEM image of the assembled nanocubes on a carbon coated Cu grid (a), their size distribution (b) and aspect ratio (c).*

the stabilizing ligand, which controls the growth by either changing the surface energy of certain crystallographic faces or due to the selective adsorption of the oleic acid molecules on different surface facets and thus promoting the shape modification of the nanocrystals.

A representative HRTEM image of a single nanocube is shown in Figure 5.3(a), consisting of a dark core of about 23 ± 1 nm surrounded by a light-colored shell, which has a thickness of about 4 ± 0.5 nm [Mas16]. Such a core-shell structure is typically formed after atmospheric oxidation of iron to iron oxide. Here, the darker contrast of the metallic iron core originates from the higher electron density in comparison with the iron oxide shell [Tru08]. However, the absence of such a contrast in some of the particles could be explained by complete oxidation. The image 5.3(a) also revealed that both shell and core have a very well crystallized structure. Figure 5.3(b) shows a Fourier transform (FT) of the high-resolution image. The square symmetry pattern indicating, that the iron oxide nanocube is viewed along the <100>zone axis. The image also indicated, that the oxide shell is epitaxial grown on the Fe surfaces with a relation of Fe[001]||γ-Fe_2O_3/Fe_3O_4[110] and Fe(100)||γ-Fe_2O_3/Fe_3O_4(100) between core and shell [Tru08, Sha07].

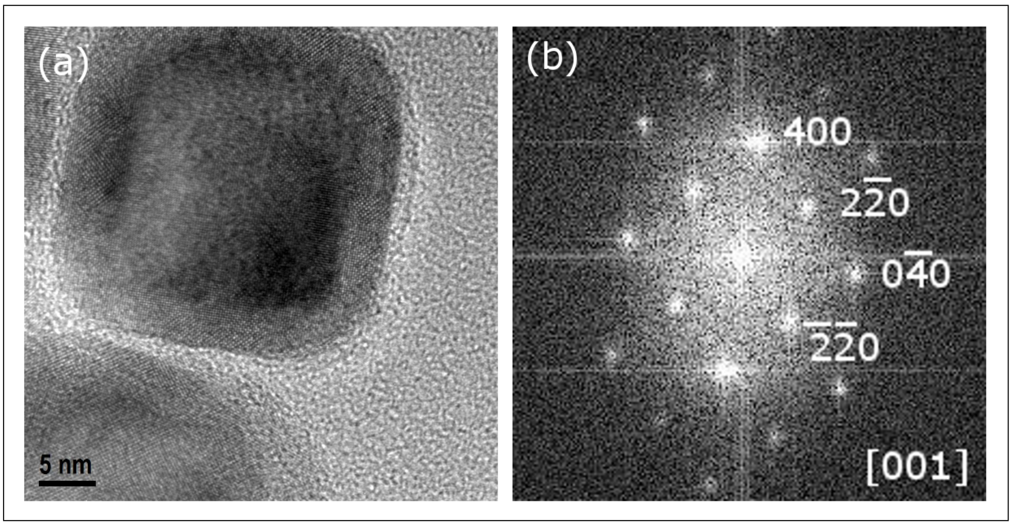

Figure 5.3: *A typical high-resolution TEM image of an individual nanocube with a core/shell structure (a) and the corresponding Fourier transform with the crystallographic indices (b).*

The combined analysis of the lattice fringe spacing and the FT image (Figure 5.3) showed that the nanocube is made of a single Fe_3O_4/γ-Fe_2O_3 crystal faceted on the six {100} planes and slightly truncated by the {110} planes.

This result was further confirmed by SAED pattern (Figure 5.4) from an assemble of nanoparticles, which illustrates the characteristic rings of a inverse spinel structure.

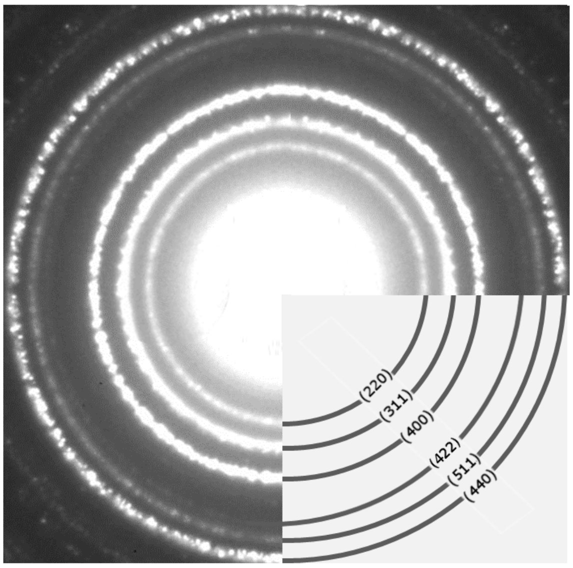

Figure 5.4: *Selected area electron diffraction pattern from an area of the sample containing several nanocubes. The hkl indices correspond to the standard atomic spacing for either* Fe_3O_4 *or* γ-Fe_2O_3*.*

The rings in the SAED image were consistent with a cubic iron oxide phase of magnetite or maghemite, with the characteristic d spacing corresponded to the hkl values, {220}, {311}, {400}, {511} and {440} [Str01]. Even though this crystal structure proves the formation of the iron oxide shell, the exact state of oxidation is very difficult to identify due to the similar crystal structure of magnetite and maghemite [Kim09]. Although it is not possible to distinguish if the oxide is either γ-Fe_2O_3 or Fe_3O_4 by HRTEM analysis alone, but several groups reported that magnetite is the usually formed oxide when taking place at room temperature [Sun04, Sim07].

In addition, the {400} and {440} interplane distances of the before mentioned iron oxides are very close to the {110} and {200} of α-Fe, respectively. Thus the corresponding diffraction rings overlap and the presence of α-Fe can neither be concluded nor excluded. However, the previously mentioned dark contrast in the particles (Figure 5.3(a)) indicates an iron core.

5.1.3 Fe_xO_y nanospheres

The second type of iron particles used in this thesis, followed the same synthesis method as the nanocubes but were kept under normal atmosphere to allow further oxidation. Figure 5.5(b) shows a TEM image of the particles, which show no dark core, indicating that the participles are indeed fully oxidized. Furthermore, the oxidation process modified the shape of the nanocubes, which now have a more spherical shape with lager and rounder truncated edges than before, as seen in Figure 5.5(a). The HRTEM image 5.5(b) shows, however, that there was no change in crystalinity or lattice parameter.

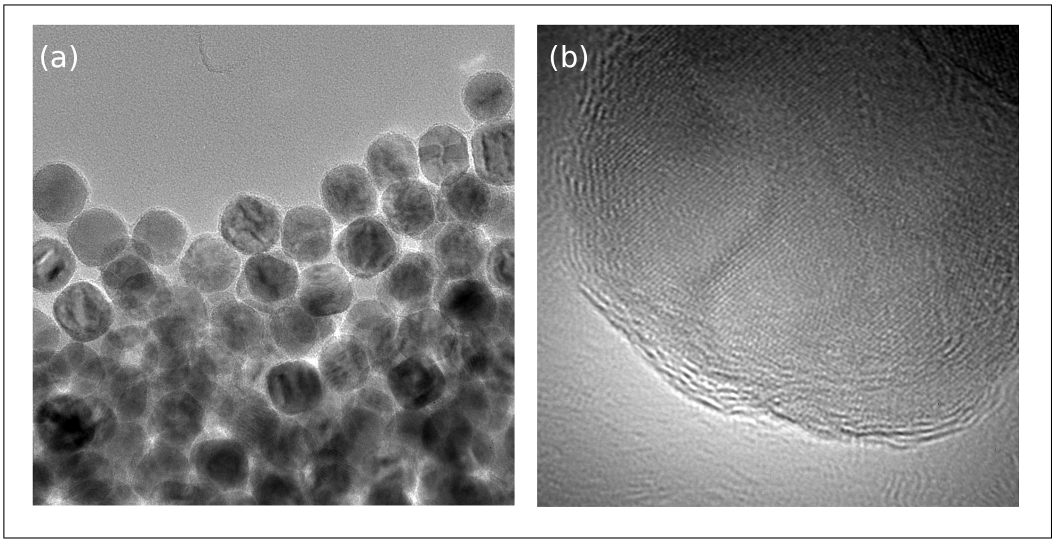

Figure 5.5: *(a) Bright-field TEM image of an assamble of nanospheres and (b) a HRTEM image of the single nanosphere. The particles are homogeniously oxidised and show no more dark iron core.*

Following the discussions of the previous section, it was not possible to distinguish if the oxide is γ-Fe_2O_3 or Fe_3O_4.

5.2 Titanium dioxide

The TiO_2 nanoparticle were synthesized and kindly provided by the workgroup ”Nanoparticle Process Technology” (NPPT) of Prof. Winterer from the University Duisburg-Essen.

Because the particles were not synthesized as part of this work, only a short overview of the synthesis process is given, but more detailed information can be found in reference [Win12]. The particles are then characterized by TEM and Raman spectroscopy.

5.2.1 Synthesis

Figure 5.6 shows a schematic drawing of the chemical vapor synthesis (CVS) setup used for the TiO_2 particle synthesis. The precursor (titanium-tetraisopropoxide) was fed into a precursor delivery system (bubbler), where it was evaporated and carried further into the hot-wall reactor by a helium stream. There the TiO_2 particles were formed in reaction with oxygen. The synthesized particles were then collected in the particle collector. Here, the particles were separated from the carrier gas and byproducts by thermophoresis.

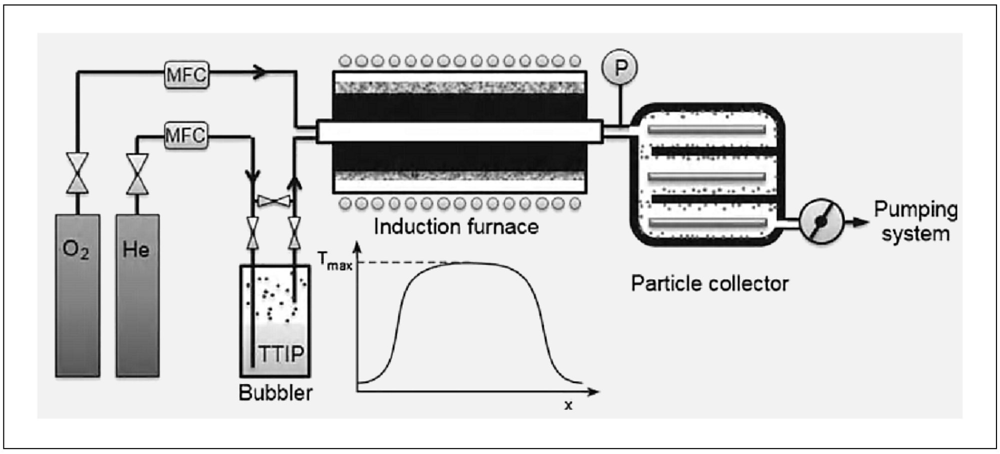

Figure 5.6: *The chemical vapour synthesis setup used for the synthesis of TiO_2 nanoparticles taken from reference [Win12].*

The main advantage of those CVS nanoparticles is their pure surface, meaning that the particles are synthesized without any surfactant molecules and thus can be used as a surfactant testing system (see Chapter 6.2).

5.2.2 TiO_2 characterization

To characterize the TiO_2-NP, the powder was dissolved in Ethanol and re-dispersed using a ultrasonic bath. The solution was then drop-casted on a copper grid and analysed using a TEM. Figure 5.7 shows a typical TEM image of the particles, revealing a more or less spherical morphology for TiO_2 nanoparticles with sizes ranging between 20 and 60 nm. The particles were not stable enough on their zone axis, therefore it was not possible to conduct a direction dependent analysis.

Figure 5.8 shows the Raman spectrum of the as-prepared TiO_2 nanocrystals. The Raman lines at 148, 196, 398, 515, and 641 cm^{-1} can be assigned to the modes of the anatase phase. However, they exhibit a small shift in frequency compared to the Raman shifts in bulk anatase [Ohs78]. Since the Raman lines become weak and broad when the sample has local lattice imperfections, one can conclude that the as-prepared nanocrystals have a good crystallinity. Moreover, the spectra confirms the absence of organic molecules on the nanoparticle surface.

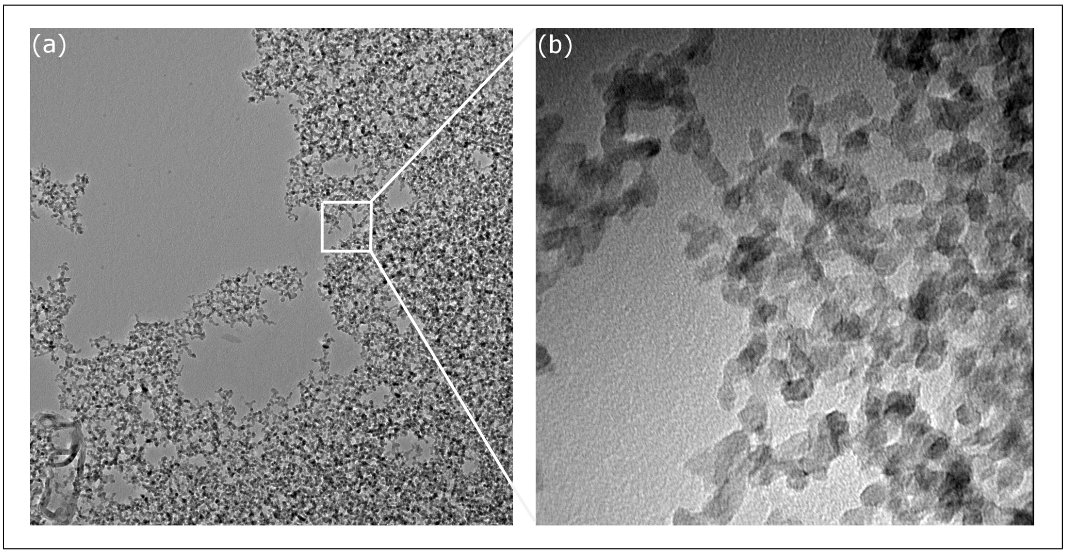

Figure 5.7: *Bright-field TEM image of TiO_2 nanoparticles synthesized by chemical vapour synthesis in two different magnifications.*

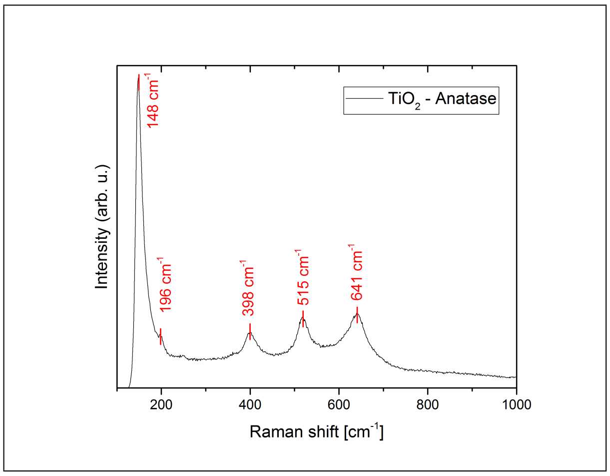

Figure 5.8: *Raman spectra of anatase* $\mathrm{TiO_2}$ *nanoparticles, without surface ligands*

6 Electron paramagnetic resonance of carboxylic acid molecules coupled to Fe-oxid

The previously described iron/iron oxide core/shell nanoparticle were drop-casted on a GaAs substrate and measured by both FMR setups. Figure 6.1 illustrates the first derivative of the imaginary part of the high frequency susceptibility χ'' as a function of the applied external magnetic field B_{ext} in the range of $200 - 400\,\mathrm{mT}$. It shows the characteristic broad ferromagnetic resonance spectrum of an ensemble of core/shell iron oxide nanoparticles at 300 K [Ter15, Tru08]. Additionally two much narrower and smaller paramagnetic resonances, S1 and S2, can be observed.

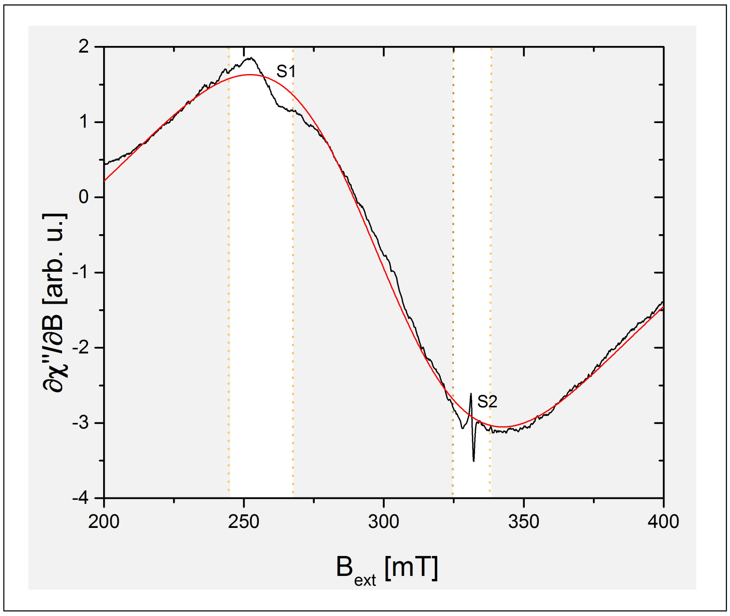

Figure 6.1: *FMR spectra of OA coated nanoparticles with two additional EPR signals arising from a partially transferred electron (S1) and a free radical (S2); the red line shows the Lorentz fit.*

Signal S1 appears at an apparent g-factor $g \approx 2.5$ with a relatively broad linewidth of approximately $17\,\mathrm{mT}$, while the second signal S2 appears at $g = 2.01$ with a narrower linewidth of about $0.65\,\mathrm{mT}$. To characterize the resonance fields, linewidths and amplitudes of S1 and S2, the broad ferromagnetic resonance line of the Fe oxide nanoparticles was fitted and subtracted as background to obtain the two EPR signals. The fit function (derived Lorentzian) is depicted in Figure 6.1 by a red line.

To test whether the two EPR signals are intrinsic for the iron particles or due to the organic molecules, single-crystalline and poly-crystalline iron oxide thin films of approximately $5-7\,\mathrm{nm}$ thickness were fabricated and covered by $5\,\mu\mathrm{l}$ OA. A representative spectra of the single-crystalline iron oxide films is shown in Figure 6.2(a). In addition to the broad FMR signal, a small EPR signal can be observed, lying at the same resonance position as the signal S2 (Figure 6.2(b)). Measurements on pure iron thin films, without oleic acid molecules showed no EPR signal at all (not shown here). Therefore, the EPR Signals can be attributed to paramagnetic centres associated with the ligand molecules attached to the nanoparticles and the iron thin film, respectively. The origin of both EPR signals (S1 and S2) will be discussed and analysed in the following sections.

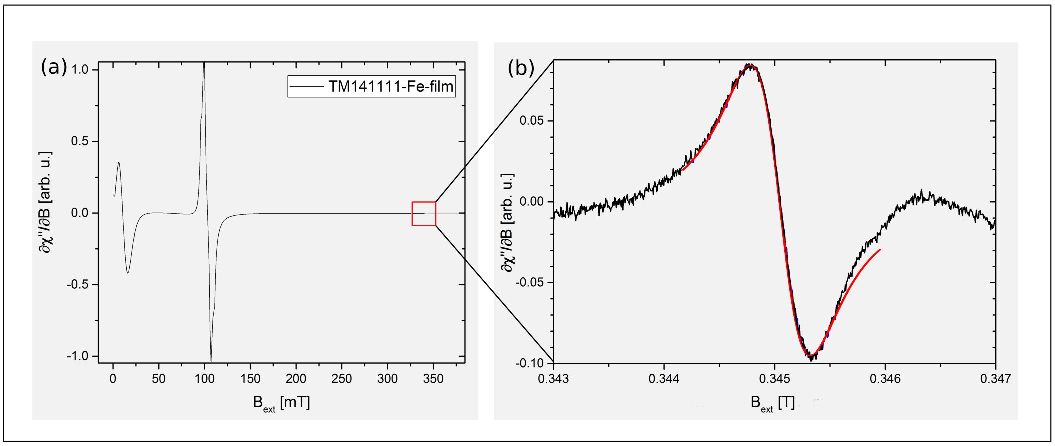

Figure 6.2: *(a) FMR spectra of an iron thin films coated with oleic acid. (b) An additional EPR signal of a free radical (S2) with a g-factor of* $g = 2.01$*; the red line shows the Lorentzian fit.*

6.1 Fourier transform infrared spectroscopy investigation on the surfactant molecules coupling mechanism

To understand the coupling mechanism of OA onto the surface of iron oxide, Fourier transform infrared spectra were recorded on both the coated nanoparticles on a GaAs substrate and poly-crystalline iron films. Figure 6.1 shows the FTIR spectrum of pure oleic acid (a) taken from the NIST database [Nis], and the nanoparticles coated with OA (b). In graph 6.1(a), the two absorption peaks at $2924\,\mathrm{cm}^{-1}$ and $2854\,\mathrm{cm}^{-1}$ can be attributed to the asymmetric CH_2 and the symmetric CH_2 stretching, respectively

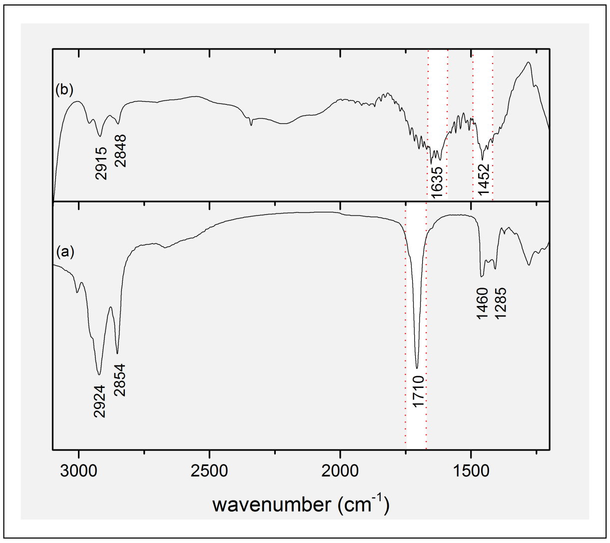

Figure 6.3: *FTIR spectra of pure oleic acid taken from the NIST database [Nis] (a) and Fe_xO_y nanoparticles coated with oleic acid molecules (b). Both spectra are not to scale on the y-axis (arb. units).*

[Nak08b]. In curve (b) those stretching modes shifted to lower frequencies (2915 cm^{-1} and 2848 cm^{-1}), indicating that the hydrocarbon chains in the monolayer surrounding the particles were in a closed-packed, crystalline state [Nak08a]. The intense peak at 1710 cm^{-1} in spectrum 6.1(a) is due to the C=O stretch vibration of the unbound COOH group, which is absent in the spectra of the coated nanoparticles (Figure (b)). Furthermore, two new bands appear at 1635 cm^{-1} and 1454 cm^{-1}, characteristic for the symmetric ν_s and the asymmetric ν_{as} stretch vibrations of the carboxylate group (COO^-), respectively. These results revealed that oleic acid is chemisorbed onto the nanoparticles as a carboxylate [Zha06].

In this work, the measured wavenumber separation $\Delta = 1635\,\text{cm}^{-1} - 1454\,\text{cm}^{-1} = 181\,\text{cm}^{-1}$ can be assigned to the bridging bidentate coupling, where the COO^- group is covalently bound to the Fe atom, as seen in Figure 2.3(c). X-ray photoelectron spectroscopy measurements conducted by different groups on similar nanoparticles coated by oleic acid molecules indicated the formation of chemical bonds between the carboxylate O atoms and the Fe atoms [Zha06, Kat99]. This coupling mechanism result in a delocalized electron at the metal surface (Chapter 2.2), which can be assumed to cause the EPR signal S1, due to the EPR signal's high g-factor of a "not-free" electron. The same coupling mechanism was found for iron thin films covered by oleic acid molecules, which are not shown here but can be found in reference [Mar16a].

6.2 Oxidation test of different acids on TiO_2 nanoparticle

As mentioned in Chapter 2.3 iron salts, such as the here used iron (II) stearate for the particle synthesis, oxidise the carboxylic acid molecules double bond [Roo07]. Thus, in order to investigate the EPR signal S2's origin further, two different carboxylic acid molecules were investigated. First, oleic acid was used as a unsaturated acid, which contains a C=C double bond and therefore tends to oxidise and form free radicals. Second, caprylic acid (CA) was used as a saturated fatty acid, which lacks any double bond and thus can't produce free radicals in the carbon chain (Chapter 2.3). Because both molecules are carboxylic acids, they both contain the same head-group as shown in Figure 6.4.

Figure 6.4: *Schematic of the two carboxylic acids used for the EPR test on* TiO_2 *(a) oleic acid and (b) caprylic acid. While both have the same head group they differ in their carbon chain.*

To obtain ligand free surfaces, TiO_2 nanoparticles were chosen because the nanoparticles were synthesized via chemical vapour deposition and thus they are free from stabilizing ligands. Additionally, titania tends to oxidise lipids and thus holds the same property as iron oxide to create free radicals [Car09]. Therefore one can use those particles for the functionalisation with different acids and the analysis of the EPR signal S2.

To verify that both molecules exhibit the same coupling mechanism to the particle surface, once again FTIR spectra were measured. Therefore, the TiO_2 particles were dispersed in ethanol, drop-casted on a glass substrate and subsequently functionalyzed by dripping $5\,\mu$l of the respective acid onto the particles. The FTIR spectrum of TiO_2 nanoparticles (Figure 6.5) shows the successful fabrication of the TiO_2-OA and TiO_2-CA composites. The presence of COO^- is again proven by two peaks at $1565\,\mathrm{cm}^{-1}$ and $1403\,\mathrm{cm}^{-1}$ and the disappearance of the peak at $1700\,\mathrm{cm}^{-1}$. This demonstrates that the carboxylic acid layer on TiO_2 is formed mainly by a chemical reaction instead of physical adsorption. It also demonstrates, that the coupling mechanism is the same for both oleic and caprylic acid. The peak in Figure 6.5 at $1664\,\mathrm{cm}^{-1}$ can be assigned to the C=C stretching mode for oleic acid. Literature shows, that the oxidation of the double results in a low signal intensity for the C=C vibration [Roo07], which is in good agreement with our measurements, indicating the presents of free radicals. This mode is absent in the spectrum of CA.

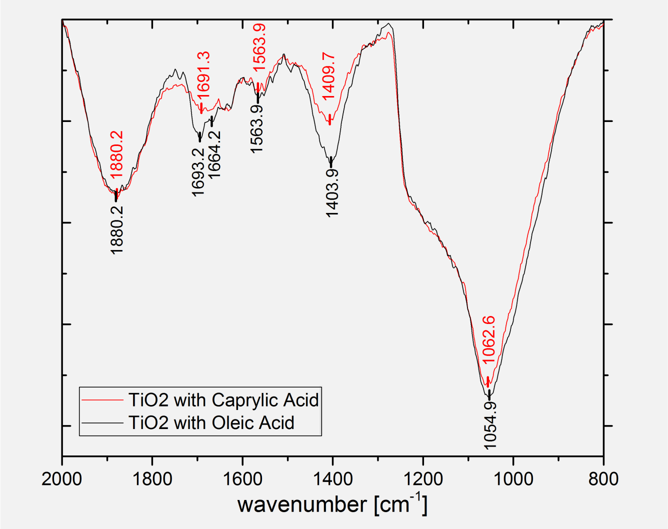

Figure 6.5: *FTIR spectra of both caprylic acid and oleic acid. The peaks at* $1565\,\mathrm{cm}^{-1}$ *and* $1403\,\mathrm{cm}^{-1}$ *show that the acids get chemisorbed into to* TiO_2*-NP surface.*

Both carboxylic acid molecules on TiO_2 were subsequently analysed by EPR measurements. Figure 6.6(a) and (b) show the measured spectra of the nanoparticles covered by oleic acid and caprylic acid, respectively. The inverse line shape is a measurement related effect, caused by a 180° phase rotation of the high frequency field. As can be seen from the two graphs, the surface modification of TiO_2 nanoparticles with carboxylic acids, which contain the same functional head group, results in a broad EPR signal. The signal for both molecules was stable over several measurements. While previous studies on titania demonstrated, that stoichiometric Ti^{4+} shows no EPR signals, this result suggests the formation of EPR active Ti^{3+} due to the carboxylate coupled to the particle. This Ti-ions are usually induced when an electron is adsorbed on Ti^{4+} [Kum06]:

$$Ti^{4+} + e^- \longrightarrow Ti^{3+} \tag{6.2.1}$$

This reduction of titania to Ti^{3+} is most likely due to the absorption of the unpaired electron of the chemisorbed carboxylate head group.

Literature indicates the existence of a substantial g-tensor anisotropy for bulk Ti^{3+}, ranging from $g = 2.035$ to $g = 1.98$ [Kum06]. The g-factor calculations at a resonance frequency of 9.568 GHz for the OA and CA coated particle, however, show factors of $g \approx 2.29$ and $g \approx 2.11$, respectively. Here one has to consider that the molecule

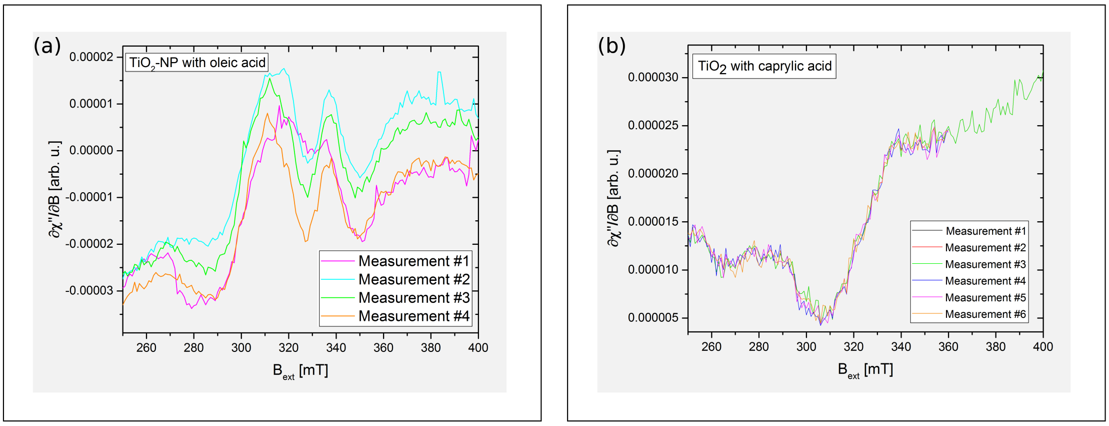

Figure 6.6: *(a) EPR spectra of oleic acid coated* $\mathrm{TiO_2}$ *nanoparticles with two EPR signals arising from* Ti^{+3}*-ions and a free radical due to lipid oxidation. (b) EPR spectra of caprylic acid coated* $\mathrm{TiO_2}$ *nanoparticles with only one EPR signal arising from* Ti^{+3}*-ions.*

generates surface Ti^{3+} ions, which differ from the bulk properties and thus might exhibit different g-factors. Furthermore the delocalized electron on the particle surface might cause an additional EPR signal. The sum of those signals might result in the broad signal linewidth of $\Delta B_{res,OA} = 28 \pm 1mT$ and $\Delta B_{res,CA} = 31 \pm 1mT$. The exact reason for this broad linewidth and difference in g-factor for the two spectra was not investigated in this work.

However, comparing the two spectra one has to note that an additional EPR signal occurs for the oleic acid covered nanoparticles, which is absent for carboxylic acid. Here, one possible explanation is that the signal arises due to the oxidation of the carbon double bond. Sayre et. al found, that the valence band holes in titania tend to oxidise the double bond in oleic acid [Say00]. Furthermore, the signal is at the approximate resonance position ($B_{res} = 344\,\mathrm{mT}$ and $g = 1.998$) as the Signal S2 in the case of iron oxide particles. Therefore, this result suggests that the EPR signal S2 is caused by a free radical originating from the oxidized double bond.

6.3 In-situ investigation of oleic acid on iron films

To investigate the impact of an oxidized surface on the EPR signal, in-situ FMR/EPR experiments were conducted. A 4x4 mm^2 GaAs (100) substrate is heated in an ultra-high vacuum chamber (1×10^{-10} mbar) up to 900 K, while being sputtered with argon ions and subsequent annealing at 900 K for 30 minutes to get a clean and crystalline surface. Afterwards an iron film is epitaxially grown on the substrate by means of electron beam evaporation at a rate of 0.7 Å/min with a thickness of approximately 4 nm.

The chemical composition was determined by AES at all phases of the sample preparation. Figure 6.7 shows Auger spectra of the three different fabrication stages. The blue spectrum represents an as-prepared iron film, which still exhibits a minor oxygen signal at 513 eV. By comparing the amplitude ratio between oxygen and iron one can estimate that less than 0.1 monolayers of oxygen are present [Far16]. This peak gained in intensity after oxidizing the film with an oxygen partial pressure of $p_{O2} = 1 \times 10^{-6}$ mbar (red spectra). Finally, the green spectrum is recorded after exposure to 5 L oleic acid on the oxidized iron film which results in a pronounced carbon signal at 273 eV. All spectra were normalized to the iron peak at 703 eV [Mar16b]. Subsequently, several Langmuir of oleic acid are deposited in-situ onto the iron films. Here, the UHV chamber had to be modified to allow the in-situ evaporation, as can be found in reference [Mar16a]. The EPR/FMR investigation was conducted at a microwave frequency of $f = 9.2$ GHz and a microwave power of 20 mW. Figure 6.8 shows the measured spectra. For the as prepared iron film, which showed a small oxygen signal prior to the oleic acid exposure, only a weak ESR signal could be detected. After the oxidation the EPR signal's amplitude was approximately 200 times larger than the one for the 'non-oxidized' iron film, as shown in Figure 6.8 [Mar16b].

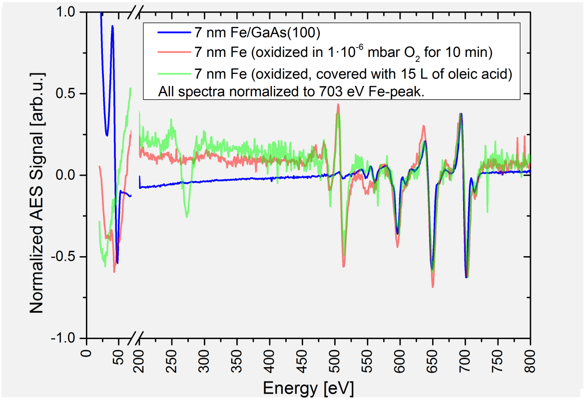

Figure 6.7: *Auger spectra in various steps of sample preparation. Blue: Fe film after growth on GaAs (100) substrate, red: the same film after oxidation, green: the same oxidized film after exposure to* 15 L *oleic acid. (Data provided by T. Marzi).*

From these in-situ measurements and FTIR spectra alone it was not possible to determine the exact origin of the EPR signal for the iron films in the framework of this thesis. On the one hand, following the theory of fatty acid oxidation from Chapter 2.3, one could conclude that the signal arises from the oxidation of the double C=C bond. On the other hand, the FTIR spectra indicated the coupling of the molecule to the iron film surface, which also results in an EPR center. A more detailed analysis on of the iron thin films can be found in reference [Mar16a].

The result of the in-situ test suggests, however, that the oxidation of the iron is mandatory to create the ESR signal. Here, the oxide acts as the electron acceptor for the oxidation of the OA.

$$\mathrm{Fe}^{3+} + \mathrm{e}^{-} \longrightarrow \mathrm{Fe}^{2+} \tag{6.3.1}$$
$$\mathrm{OA} \longrightarrow \mathrm{OA}\cdot \tag{6.3.2}$$

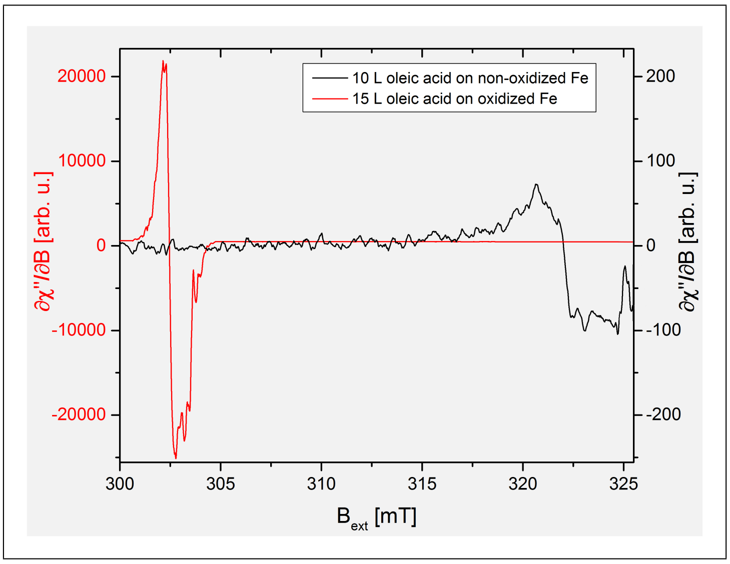

Figure 6.8: *EPR spectra of the pure (black line) and oxidised (red line) iron film covered with oleic acid. The EPR signal's amplitude of the oxidized iron film is approximately 200 times larger than for the non-oxidized iron film. (Data provided by T. Marzi).*

6.4 Auto-oxidation test on two carboxylic acids

To exclude the possibility of auto-oxidation due to exposure to either air or daylight, the two different carboxylic acids were tested on EPR signals without any contact to iron or TiO_2. Therefore, $5\,\mu$l of either OA or CA were put into open glass pipettes and were exposed to air and sun radiation for two weeks. Figure 6.9 shows the long-term EPR measurements of (a) oleic acid and (b) caprylic acid. Comparing the empty cavity measurement (black graph) with the measurements of the respective acid after two weeks of exposure to air and sun radiation (red graph) showed that there was no measurable amount of radicals in the acids. To go one step further, the acids were again measured while exposed to a mercury vapour lamp (blue graph) to force radicals to form, but there was no EPR signal detectable. Those measurements suggested that the EPR signal's origin is indeed related to a chemical reaction with the sample system.

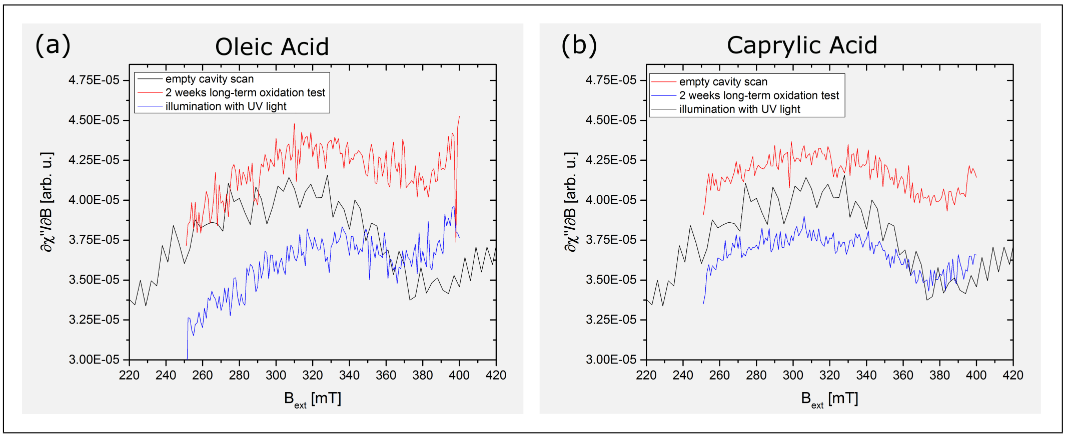

Figure 6.9: *Long-term oxidation EPR test of (a) oleic acid and (b) caprylic acid. The graph shows the empty cavity measurement (black graph), the measurement after two weeks of exposure to air and sun radiation (red graph) and a measurement while exposed to a mercury vapour lamp (blue graph). There was no measurable amount of radicals found in the acids for all cases.*

6.5 Origin of the paramagnetic resonance signals of iron oxide nanoparticles

This section will give a short overview on the principal theory of the EPR signal's origin based on the results and observations in the previous chapters.

The broad EPR signal S1 can be attributed to a chemical reaction, which takes place in the synthesis process due to the molecules coupling mechanism to the particle surface when high temperatures (as high as 350 ° [Wil05]) are involved. Here the electron is not free but partially transferred between the molecule and the metal surface (Fig. 6.10 S1). This chemisorption induced partial electron (i.e. spin density) redistribution further results in an enhanced relaxation channel and a larger EPR linewidth as a free radical.

Furthermore, unsaturated fatty acid moieties, like oleic acid, tend to oxidise in the presents of active oxygen-iron complexes a free radical is formed by removing a labile

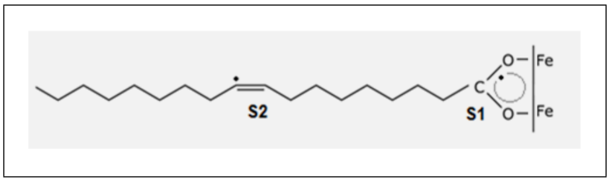

Figure 6.10: *Model of the EPR signal's origin. The coupled molecules has to EPR centers arising from a partially transferred electron (S1) at the carboxylate head group and a free radical (S2) in the carbon chain.*

hydrogen from a carbon atom adjacent to a double bond. Therefore, the second EPR signal S2 most probably originates from an uncoupled paramagnetic species in the chain of the molecule (Fig. 6.10 S2). This oxidation induced radical could also be observed for TiO_2-NP.

This model provides a reasonable interpretation and understanding of the experimentally observed EPR signals. Is is used in the following discussions of the experiments.

7 Applications

The following chapter will briefly discuss some possible applications for the oleic acid molecule as an EPR marker. Firstly, temperature dependent measurements were conducted, which indicated that the molecule might be used as surface temperature probe. Secondly, angular dependent FMR and EPR experiments showed the possible use as a method for probing the magnetic stray field on the nanoparticle surface [Rak04].

7.1 Surface sensitive temperature probe

As part of this thesis the use of the functionalized iron oxide particles for biomedical application is investigated. Here one application is an approach to determine the temperature of the surface of a nanoparticle for the implementation in hyperthermia procedures.

To measure the temperature dependent behaviour of the EPR signals, the sample was cooled and heated in a nitrogen gas flow. To minimize the error of the experiment, the sample had time to equilibrate for 15 minutes after the desired temperature was reached and before the respective measurement was started. Thus the error in temperature is less than $\pm 0.2\,\mathrm{K}$ and is not shown in the following diagrams. All the data were evaluated after the subtraction of the FMR line and by applying a derived Lorentzian fit-function to the respective signal, as already seen in Figure 6.1. Unless otherwise stated, the error bars in the following plots are given by the residuum of the fit functions, determined by Mathematica.

Figure 7.1(a) and (b) shows the temperature dependent resonance field and linewidth of the FMR signal, respectively. These data show that the core/shell particles exhibit the behaviour of a superparamagnet above room temperature which is near its blocking temperature [Mas16]. Due to the very short time window in the range of nanoseconds for FMR measurements, the apparent blocking temperature is increased [Owe05, Ant05], which consequently results in the temperature dependent effects of dipolar coupling (magnetization) and magnetic anisotropy influencing the resonance field and the linewidth. The small jump around $335\,\mathrm{mT}$ is a metrologically related error whereby the sample temperature was not stable but slightly higher (estimated error $4 \pm 1\,\mathrm{K}$) than anticipated.

Figure 7.2 shows the temperature dependence of the EPR signal S1 between $250\,\mathrm{K}$ and $350\,\mathrm{K}$. The graph clearly illustrates a shift in resonance position to higher fields

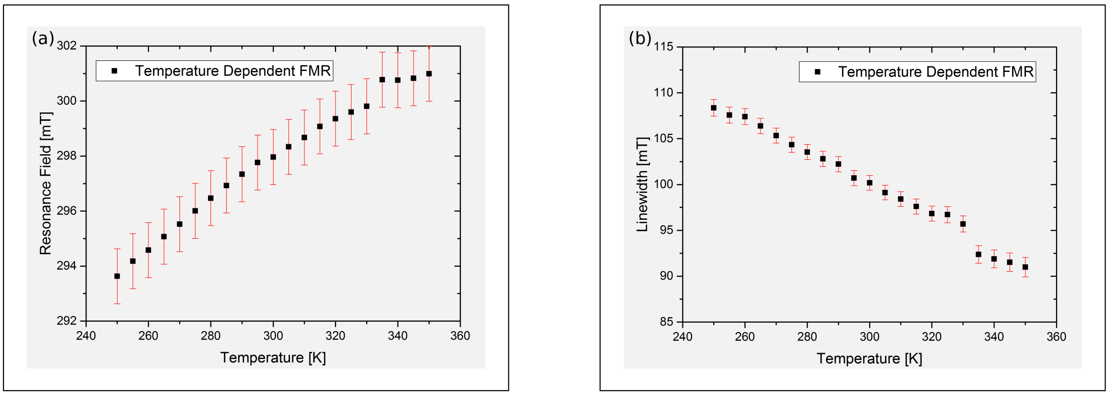

Figure 7.1: *Temperature dependent shift of the resonance field (a) and linewidth (b) of the FMR signal of the nanocubes. The small jump around 335 mT is a metrologically related error.*

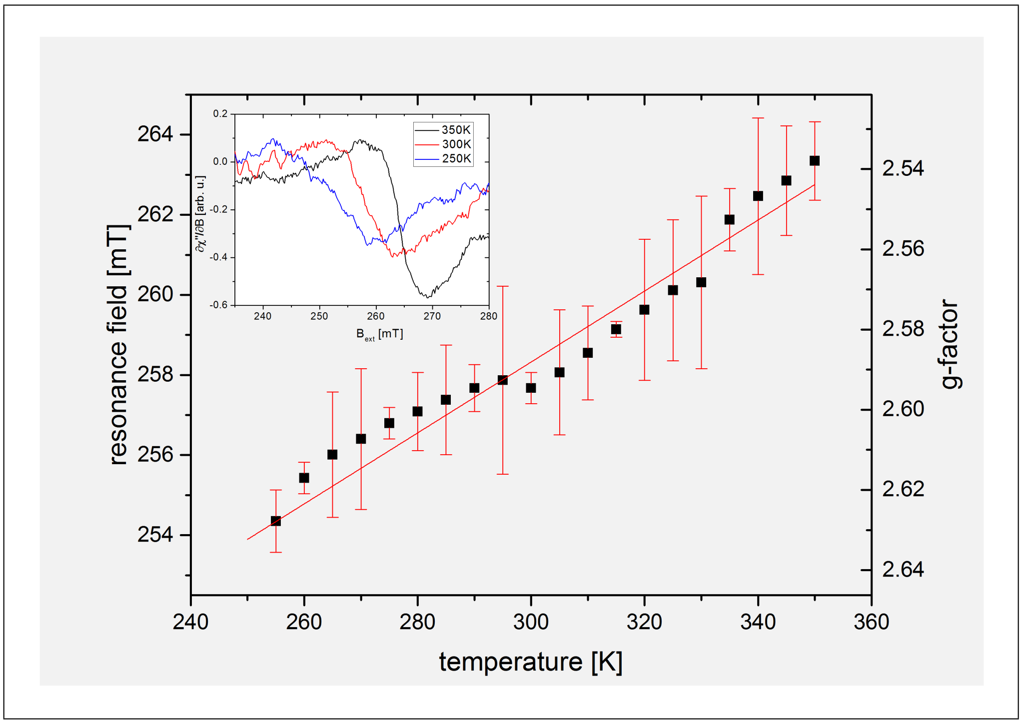

Figure 7.2: *Resonance field position and g-factor calculation of the EPR signal S1 from the coupled oleic acid molecule for a resonance frequency of 9.53 GHz. The inset shows the EPR signal S1 after FMR signal subtraction.*

with a rate of approximately 0.1 mT/K as the temperature increases, which corresponds to a change in magnetisation of about 80 A/m (for a maximal assessment of μ_0). Such a behaviour is not expected a priori for a normal paramagnetic resonance, such as a free radical. Moreover, the temperature dependent shift towards the g-factor g = 2 of a free electron and the broadened resonance which indicates higher relaxation rates supports the model of a partially transferred electron directly at the interface between nanoparticle and oleic acid. Following this model, the transferred electron at the particle surface can be influenced by small changes in its surroundings. Thus, this shift is expected for the previously mentioned temperature dependent decrease of the magnetization (or stray field) and magnetic anisotropy at higher temperatures [Owe05, Ant05]. This effect is confirmed in the following Chapter 7.2, which shows that the signal S1 is greatly influenced by changes in the particles' stray field.

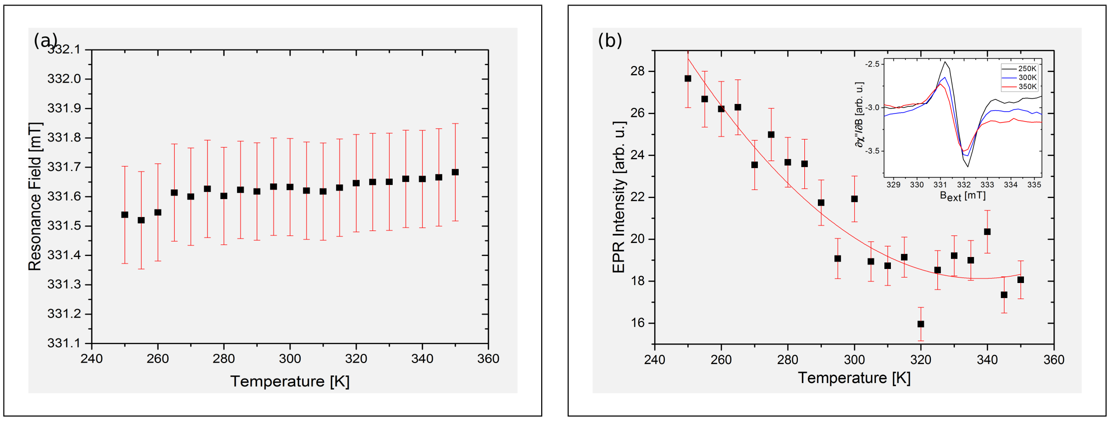

Figure 7.3: *Temperature dependence of the EPR signal S2. The resonance field position is constant over the whole temperature range and the intensity illustrates a Curie-law-like behaviour. The inlet in (b) shows the measured S2 signal.*

It is apparent from Figure 7.3(a), that the signal S2 does not show a temperature dependent change of the resonance field but has a stable g-factor of g = 2.015±0.001 over the whole temperature range. This result is an indication that this signal results from a paramagnetic centre in the oleic acid carbon chain (double bond C=C), as assumed in Chapter 6.5. Due to its lager distance of approximately 1 nm from the particle-molecule interface, the signal is ,if at all, only weakly influenced by the temperature induced changes in magnetic stray field. Additionally the decrease in EPR intensity of signal S2 in Figure 7.3(b) illustrates a Curie-law-like behaviour. Here, the intensity of the EPR signal is calculated using the following equation:

$$I = \frac{\Delta A_{pp}}{\Delta B_{pp}^2} \tag{7.1.1}$$

where ΔA_{pp} is the peak-to-peak amplitude and ΔB_{pp} the peak-to-peak linewidth. The reported intensity values are in an arbitrary scale. The red line in the figure is just a guide to the eye given by a non-linear fit and no Curie-law function. For a more detailed analysis of the temperature dependent intensity of an EPR signal one can consult reference [Gri99].

In summary, our measurements not only support the model of the EPR signals' origins, but it also demonstrates the possible use as a non-invasive surface sensitive temperature probe. Here we suggest using the shift in resonance field position of the EPR signal S1 in the carboxylic molecule attached to the particle's surface as a temperature monitor for e.g. hyperthermia application.

7.2 Surface sensitive stray field detector

A second possible application, is the use of angular dependent FMR and EPR measurements to determine the particles stray field. Thus two different types of angular-dependent measurements were performed:

- azimuthal (ϕ_B) angular dependence when the external field was rotated in the sample plane and
- polar (θ_B) angular dependence when the applied field was rotated in a plane normal to the film plane

as can be seen in Figure 7.4. All following angular dependent ferromagnetic resonance measurements were carried out at 9.5 GHz and 300 K.

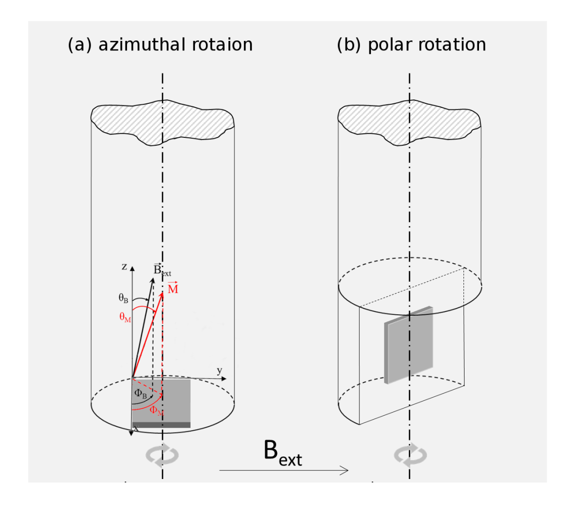

Figure 7.4: *Sketch of the two arrangements for the azimuthal (a) and polar (b) angular dependent measurements on two different sample holders. The z-axis of the sample coordinate system is parallel to the sample normal for both arrangements. The sample itself is represented by the dark grey rectangle.*

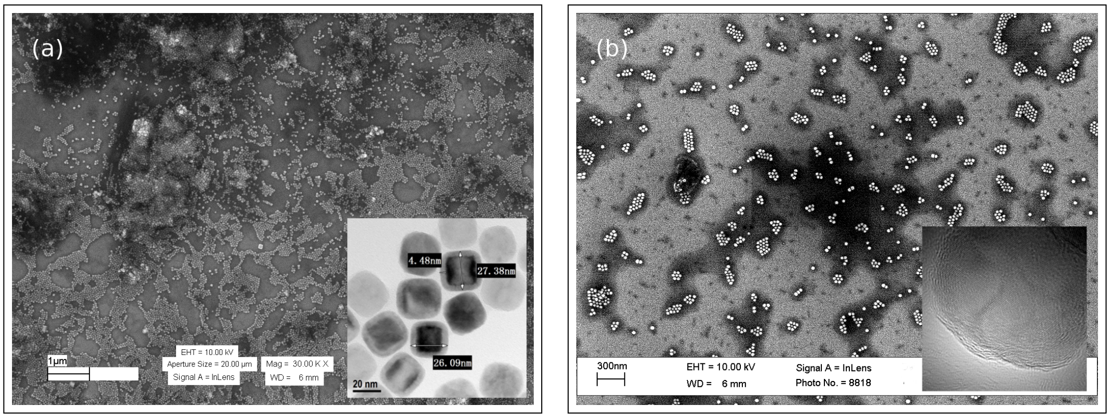

Figure 7.5: *Overview SEM images for both cubic (a) and spherical (b) nanoparticle arrangements on GaAs substrates. The insets show the respective particle morphology.*

To prove the molecules application as a stray field sensor, two different samples with oleic acid covered iron oxide nanoparticles were analysed, which have either cubic or spherical shape and were previously described in Chapter 5. Those two NP samples should exhibit a distinct morphology-induced difference in stray field. To conduct the magnetic characterization the nanoparticles were deposited onto a GaAs substrates. Subsequently, the particle arrangements were investigated by SEM to later correctly interpret the results. Figure 7.5(a) and (b) show the SEM image of the iron nanocubes and the iron oxide nanospheres, respectively. Both form an incomplete two dimensional layer in the xy-direction and only one nanoparticle height in z-direction. The picture further shows, that the cubes exhibit a random distribution of anisotropy axes for the in-plane arrangement but form an ordered array for the out-of-plane direction, under the assumption that the particles lie on a $\{100\}$ [Tru08]. The samples were then measured as a function of both polar and azimuthal angle.

7.2.1 Angular-dependence of cubic core/shell particles

In this section the angular dependence of the cubic nanoparticles is analysed. Therefore in-plane measurements and simulations are discussed and the azimuthal angular measurements are briefly examined.

Polar angular dependence

Figure 7.6 show a grey-scale plot of the polar angular dependence of the nanocubes, when the applied external magnetic field was rotated between $0\,°$ to $180\,°$ in a plane normal to the film plane. The plot shows the external magnetic field over the polar angle. Because the grey-scale represents the signal intensity in arbitrary units it is not given here. Note that black represents the minimal and white the maximal signal amplitude.

The plot clearly shows an angular dependence for both FMR and signal S1 (S1 is indicated by a red arrow in Figure 7.6). Due to the small intensity of the signal S2 it is not visible in the plot. Thus, to get a better access to the measurement data the FMR signal was subtracted from the EPR signals and all signals (FMR, S1, S2) were fitted using the derivative of a Lorentzian function. Unless otherwise stated, the error bars in the following plots are again given by the residuum of the fit functions.

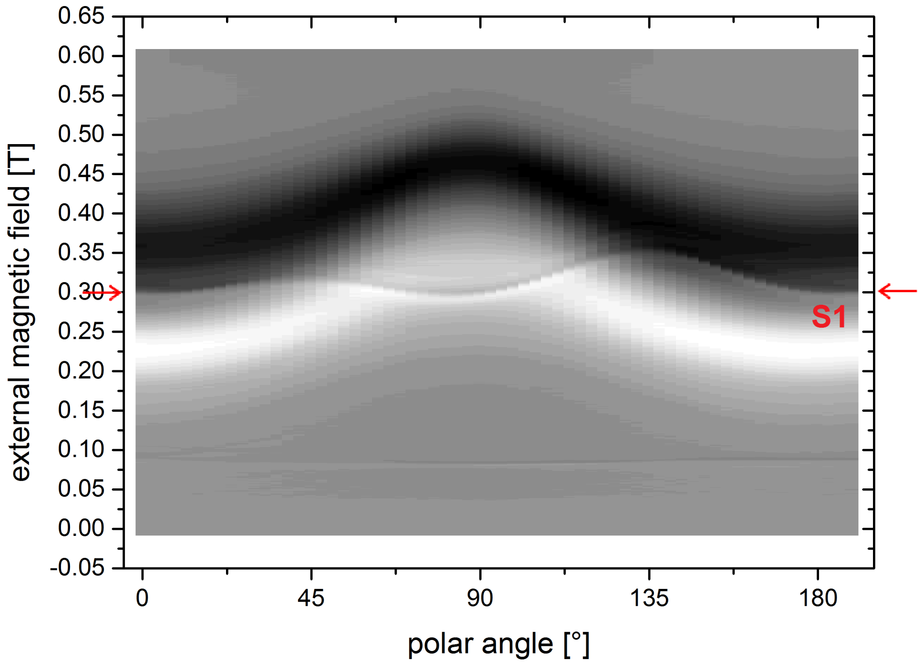

Figure 7.6: Grey-scale plot of the polar angular dependence of the OA coated iron/iron oxide nanocubes. The EPR signals S1 is marked by the red arrow. Due to the small intensity of the signal S2 it is not visible.

The first thing to note in both Figure 7.6 and 7.7(a) is the uniaxial anisotropy of the FMR signal. This can be explained by considering that the nanoparticles form an incomplete two dimensional layer, as could be seen in Figure 7.5(a). Therefore, the dipole-coupled particles exhibit a thin film like behaviour having the easy axis in-plane and the hard axis out-of-plane, which is consistent with the measurements where zero degree corresponds to the in-plane direction.

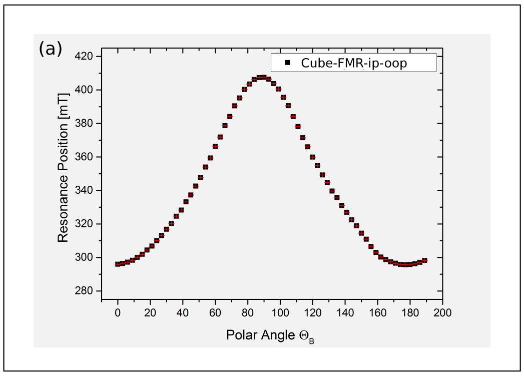

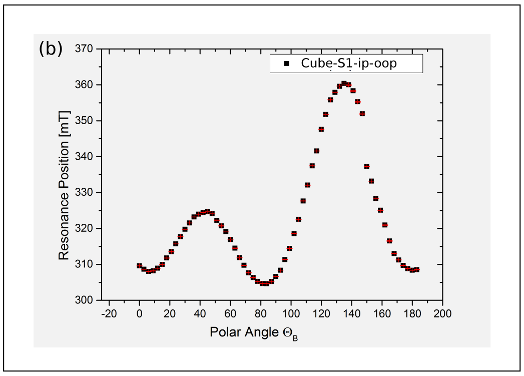

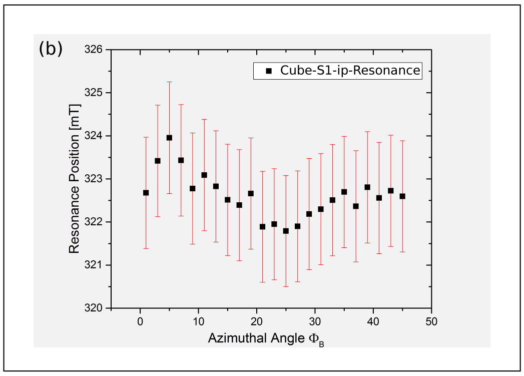

Figure 7.7: *Data evaluated by Lorentzian fits of the polar angular dependence of the iron/iron oxide nanocubes. (a) Polar angular dependence of the resonance field for (a) the FMR signal, which shows a uniaxial anisotropy, (b) the EPR signal S1 and (c) the EPR signal S2.*

Furthermore, the grey-scale plot in Figure 7.6 shows an angular dependent resonance field for signal S1, which seems like a four fold anisotropy with the hard axis corresponding to the out-of-plane angles of 45° and 135°. This tendency is also seen in the data in Figure and 7.7(b). This graph illustrates the exact change in resonance position over the angle, ranging from 304 mT to maximum of 360 mT. This variation in resonance field of S1 can be attributed to an angle dependent change in the effective magnetic field, influencing the EPR signals' resonance position, as later qualitatively confirmed by micro-magnetic simulations. Furthermore one should note the different resonance fields for the angles 45° (324 mT) and 135° (360 mT), which differ by 36 mT. This might be caused by a superposition of an uniaxial anisotropy [Far16]. An estimate of its magnitude is the before mentioned difference of the resonant field at 45° and 135°. The exact reason for those different resonance field could not be determined in this thesis.

The data fits in Figure 7.7(c) illustrate that there is no measurable change in resonance field position for the signal S2. Thus the angular dependent change in stray field is to weak to cause variations in the effective magnetic field and influence the free radical in the carbon chain.

Micromagnetic stray field simulations for cubic core/shell particles

To better understand why there is a the change in resonance position for the signal S1 in the nanocubes but not for the nanospheres (Chapter 7.2.2), micro magnetic simulations were conducted by Thomas Feggeler of the workgroup Farle using the program MuMax3 [MuM]. Here, thanks to the previously described TEM analysis of the particles composition, a model of a core/shell nanoparticle was developed, consisting of a 30 nm iron core and a 5 nm magnetite shell and dimensions of 40x40x40 nm with truncated corners. The details of this simulations and the program can be found in reference [Feg16]. In this thesis only two simulated planes are discussed. Firstly a plane in the middle of the NP and secondly a plane 1 nm above the NP surface at the position of the free radical in the molecules carbon chain.

Figure 7.8 and 7.9 show the resulting plots for the magnetic stray field inside and outside on top of the nanocubes. The density of lines outside the particle represents the fields magnitude. The left row (Figure 7.8) illustrates the field in the middle of the particle for the angles 0°, 30° and 45°. Those simulations show, that the magnetic field inside and outside the particle is not homogeneously aligned over the whole angle measurement. By rotating the core/shell cubes the stray field directly at the particle surface change with respect to the angle and reaches an extrema at 45°. At this angle the direction of magnetization inside the iron oxide shell is at an angle of approximately $30 - 35°$ in respect to the magnetization in the iron core. Thus, the effective magnetic field acting on the surface sensitive EPR probe changes, leading to the angular dependent shift in resonance position. Moreover, simulations and measurements indicate, that the magnetization of the whole particle is most uniformly aligned for 0° and 90° and thus less external field is needed to fulfil the resonance condition creating a minima in the resonance position. On the other hand, the magnetization is most strongly misaligned at at 45°. Therefore more external field is needed, which is represented by the maxima in the resonance field.

Figure 7.9 show the plots for the magnetic stray field 1 nm above the nanocubes surface. The hexagonal shape is caused by the before mentioned truncated edges of the cube. This distance was chosen because, according to the theory presented in Chapter 6.5, the molecules double bond oxidises creating a free radical approximately 1 nm in the carbon chain. The simulations show, that the stray field is homogeneous over the whole area. Meaning, that there is no change in the effective magnetic field acting on the free radical on top of the nanocube. Thus there should be no detectable change in resonance position, which is in good agreement with the before discussed results in Figure 7.7(c).

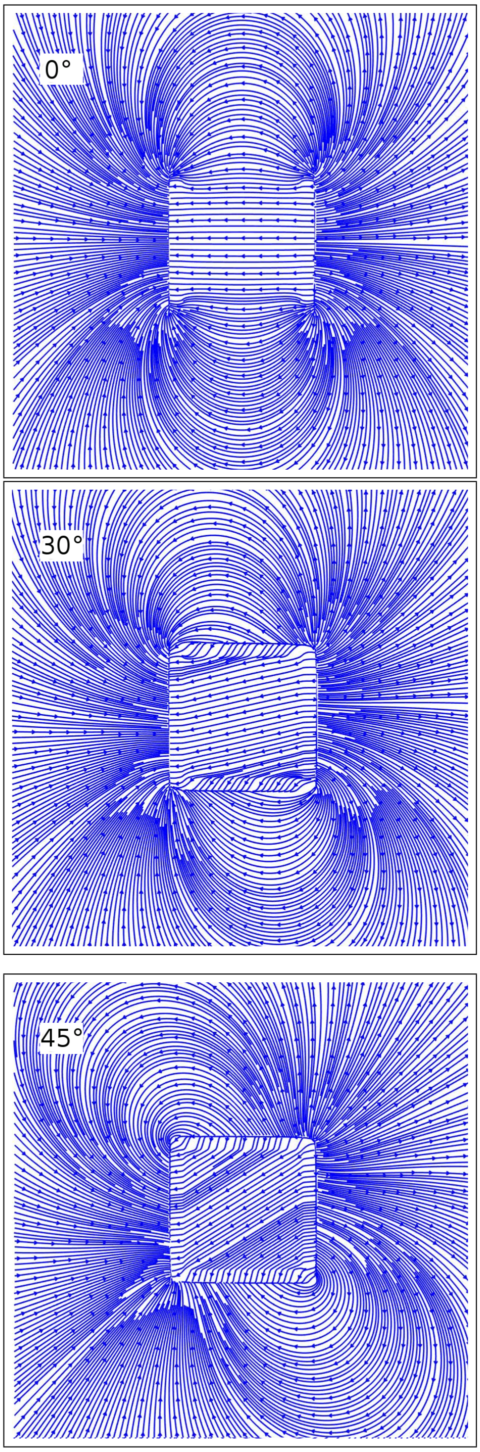

Figure 7.8: *MuMax3 simulations of the magnetic stray field in the middle of the nanocube for the angles* 0°, 30° *and* 45°.

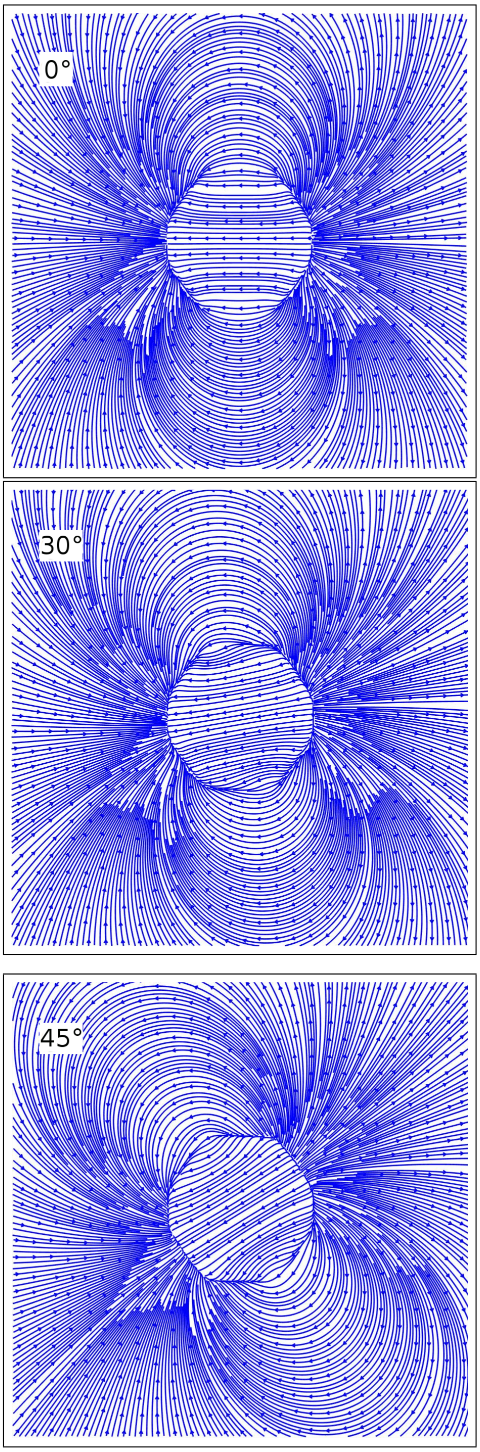

Figure 7.9: *MuMax3 simulations of the magnetic stray field 1 nm above the particle surface for the angles* 0°, 30° *and* 45°.

Azimuthal angular dependence

For completeness, azimuthal angular dependent measurements of the nanocubes were conducted. As can be seen in Figure 7.4(b) the particles have a random orientation. Figure 7.10 shows the grey-scale plot of the external magnetic field over the azimuthal angle. For this measurement, the azimuthal angle ϕ_B was measured from starting parallel to the in-plane easy axis. Due to the relatively big sample size of 4x4 mm the in-plane rotation only 45° could be measured.

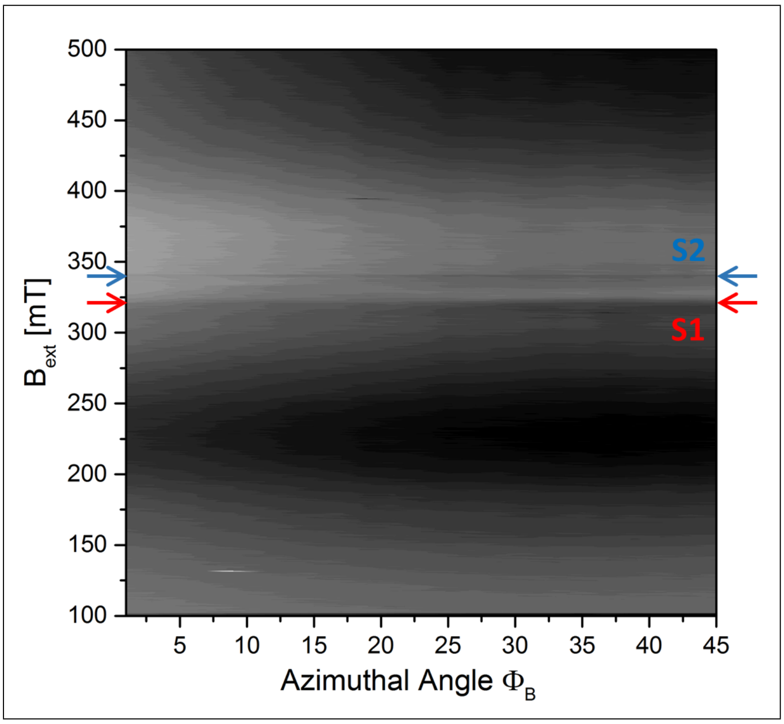

Figure 7.10: *Grey-scale plot of the azimuthal angular dependence of the resonance field for oleic acid coated iron/iron oxide nanocubes. The two EPR signals S1 and S2 are marked by the red and blue arrow, respectively.*

From Figure 7.10 and the respective data fits (Figure 7.11) it is evident that no angular dependence was observed. The resonance field of neither the FMR (Figure 7.11(a)) nor the two EPR (Figure 7.11(b) and (c)) signals change in resonance position in the range of the error. Considering a random distribution of anisotropy axes in the sample plane, as anticipated by the previously discussed SEM images, this angle independent resonance field was to be expected. The measured linewidth of 77 ± 1 mT for the FMR, has a value between the previously discussed easy and hard axis, indicating a distribution of randomly orientated nanoparticle for the in-plane direction.

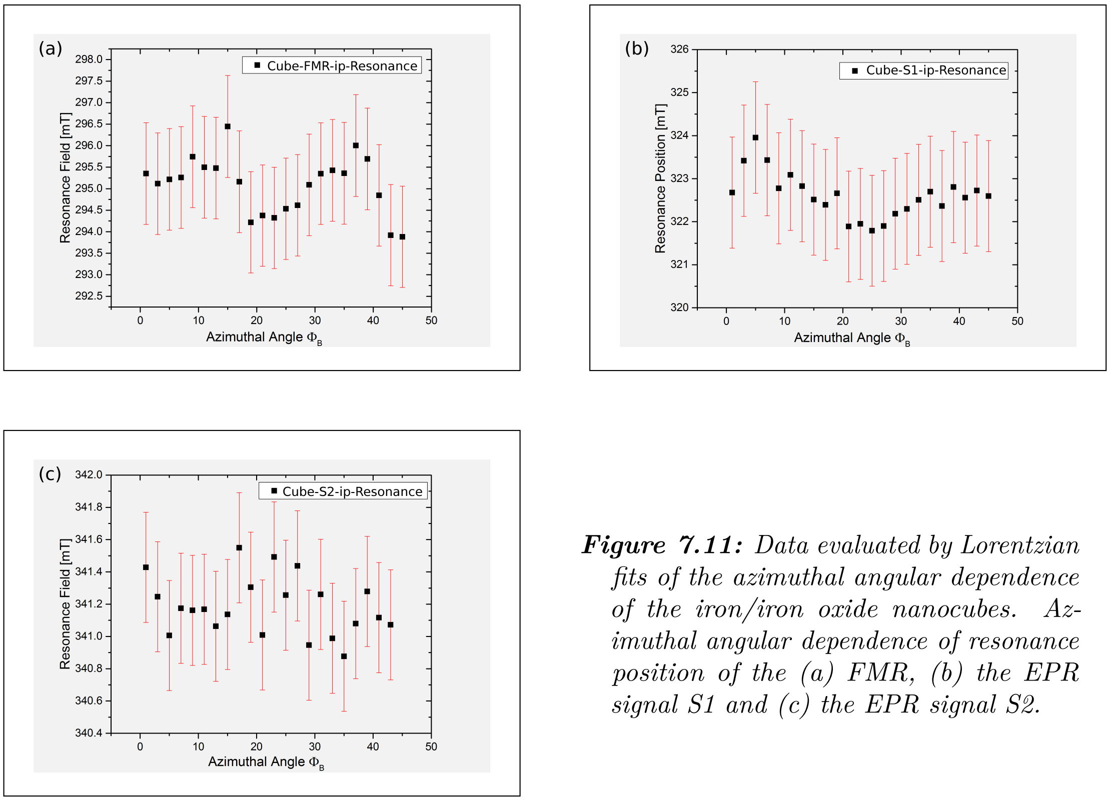

Figure 7.11: *Data evaluated by Lorentzian fits of the azimuthal angular dependence of the iron/iron oxide nanocubes. Azimuthal angular dependence of resonance position of the (a) FMR, (b) the EPR signal S1 and (c) the EPR signal S2.*

7.2.2 Angular-dependence of spherical iron oxide particles

In order to further investigate the angular dependent behaviour of the two EPR signals, other particles with a more spherical shape were measured. The previously described TEM analysis (Chapter 5.1.3) showed that those particles are totally oxidized and thus don't have a core/shell structure. Figure 7.12 shows the grey-scale plot of the polar angular dependence of the oleic acid coated iron oxide nano spheres from 15 ° to 355 °.

Due to the small intensity of the signal S2 it is again not visible in Figure 7.12, but the data fits in Figure 7.13(c) prove, that there is again no measurable change in resonance field position for the signal S2. Thus the stray field does not influence the free radical in the carbon chain. The resonance field position of signal S1 in the grey-scale plot (Figure 7.12) is stable over the angular measurement at approximately 289.5 mT.

As already discussed in Chapter 7.2.1, the FMR exhibits again a two fold symmetry. This can again be explained by considering the nanoparticle layer as a thin film. Thus, it can be seen from the resonance field position, that the measurement was not started with the external field aligned parallel to the film plane but was a little bit tilted. From these measurements alone it is not clear if the difference in stray field

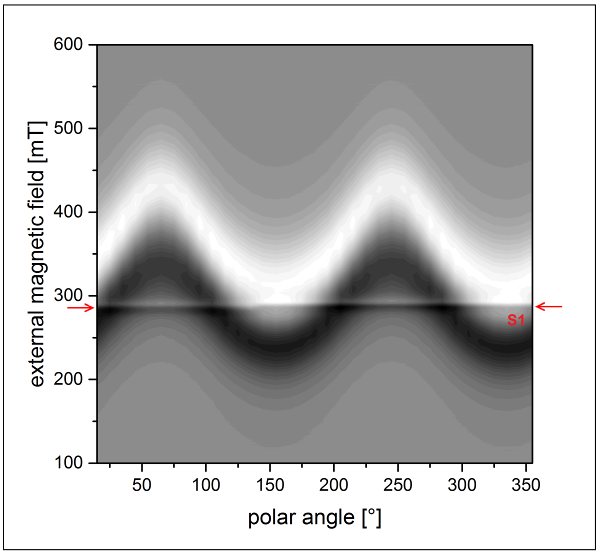

Figure 7.12: *Grey-scale plot of the polar angular dependence of the OA coated iron oxide nanospheres. The EPR signal S1 is marked by the red arrow. Due to the small intensity of the signal S2 it is not visible.*

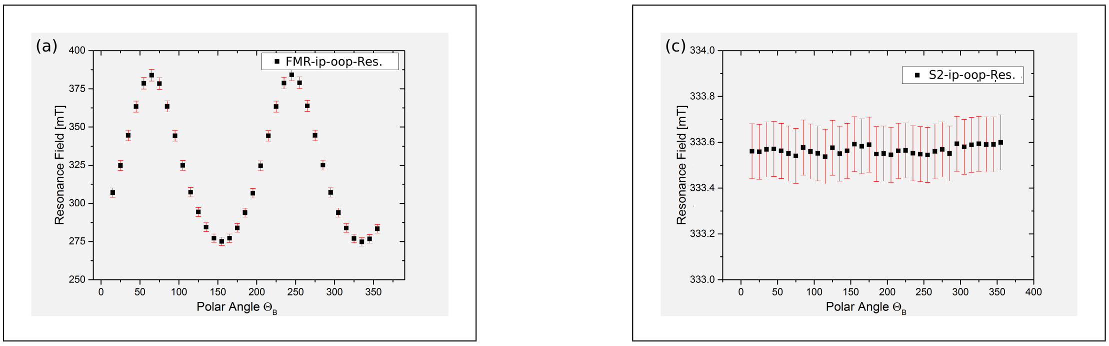

Figure 7.13: *Data evaluated by Lorentzian fits of the polar angular dependence of the resonance field of iron oxide nanospheres. (a) Polar angle dependence of the FMR signals resonace field, which shows an uniaxial anisotropy. (b) Angle dependence of the EPR signal S1's and (c) S2's resonance field.*

distribution between the spheres and the cubes originates from the spherical shape of the nanoparticle or from the lack of the core/shell structure. However, according to the simulations the absence of the core/shell structure is the most probable reason. Either way, the molecule could detect the a small changes in magnetization of the nanocubes. Thus, the here presented measurements yield a new approach to measure the stray field at the surface of nanoparticle.

8 Conclusion

In the framework of my thesis, the correlation between surfactant molecules and iron oxide nanoparticles was investigated. It was shown that due to the molecule-surface coupling and due to the oxidation of the molecules double bond, two EPR signals occur. With the evaluation of the shift in resonance field position of those EPR signals, it is possible to determine the surface temperature and changes in the magnetisation of the nanoparticles.

This thesis shows the coupling mechanism between oleic acid surfactant molecules and iron oxide nanoparticles. Here infrared spectroscopy measurements confirmed that functional groups of the oleic acid is chemisorbed as a carboxylate on the iron oxide and is coordinated symmetrically to the iron atoms. In-situ EPR experiments on pure and oxidized iron film with OA, indicated that for this coupling to occur, it is mandatory to have an oxide at the surface.

For the interpretation of the FMR and EPR results it has been mandatory to characterize the morphology and crystal structure of iron nanoparticles. Therefore HRTEM measurements were performed, which show that the nanoparticles have an iron/iron oxide core/shell structure with a cubic morphology and an average size of about 30 nm. The thickness of the oxide shell was determined to be 4.5 nm. The particles which were longer (approximately 1 year) exposed to air showed a more spherical shape and were entirely oxidized.

The FMR and EPR experiments showed the expected broad FMR signal for iron oxide cubes and two additional electron paramagnetic resonance signals arising from the coupled molecule. The first EPR signal (S1) appears at an apparent g-factor $g \approx 2.5$ with a relatively broad linewidth of approximately 17 mT. The second signal (S2) appears at $g = 2.01$ with a narrower linewidth of about 0.65 mT. By conducting infrared spectroscopy measurements it was shown that the a broad signal S1 can be attributed to a chemical reaction, which leads to the binding of the molecule to the particle surface, where an electron is partially transferred (delocalized) between the molecule and the metal surface. Furthermore, in-situ EPR on pure and oxidized iron film with OA confirmed that for the coupling to occur, it is mandatory to have an oxide at the surface. By covering TiO_2 with different carboxylic acid molecules we could conclude, that the signal S2 most probably originates from an uncoupled paramagnetic species in the chain of the molecule, which forms due to lipid oxidation.

As a result of my investigation I found two possible applications for the molecules as a surface sensitive paramagnetic probe. Via the evaluation of the shift in resonance field position for the two signals (S1 and S2) it can be seen that the molecules may be used as a non-invasive surface sensitive probe to measure the temperature of nanoparticles in a biological environment. Signal S1 gives a direct measure of the particles' surface temperature from the calibration of the resonance field with an accuracy of approximately 0.1 mT/K, which correlates to a change in magnetisation of about 80 A/m (see Chapter 7.1). In principal signal S2 yields the same information by exploiting the temperature dependent change of the susceptibility. Unfortunately a quantification of the magnetic susceptibility was not possible for the experiments conducted in this thesis, but future experiments should be able to quantify the amount of nanoparticles and attached oleic acid molecules.

With angular dependent measurements on different particle morphologies it could be show that it is possible to use the EPR signals as a surface sensitive magnetic stray field detector which can also detect small variations in the magnetization (see Chapter 7.2). This stray field and magnetization dependence was further verified by analysing the stray field distribution of a simulated iron/iron oxide core/shell nanocube obtained from micromagnetic simulations. The results are in good agreement with the experimental behaviour.

List of Figures

Bibliography

[Ant05] C. Antoniak, J. Lindner, M. Farle. *Magnetic anisotropy and its temperature dependence in iron-rich Fe_xPt_{1-x} nanoparticles.* Europhysics Letters Volume 70(2): p. 250 (2005), DOI: 10.1209/epl/i2004-10485-9 .... 49, 51

[Ant07] C. Antoniak. *Magentische Eigenschaften des Legierungssystems Fe-Pt / Volumenmaterialien und Nanopartikel.* PhD thesis, University Duisburg-Essen (2007) 20, 25

[Bra87] J. M. Braughler, R. L. Chase, J. F. Pregenzer. *Oxidation of ferrous iron during peroxidation of lipid substrates.* Biochim Biophys Acta Volume 921(3): p. 457 (1987), DOI: http://dx.doi.org/10.1016/0005-2760(87)90072-5. Braughler, J M Chase, R L Pregenzer, J F eng NETHERLANDS 1987/10/17 Biochim Biophys Acta. 1987 Oct 17;921(3):457-64. 11

[Bru] Bruker. *EPR Accessories Brochure.* URL `https://www.bruker.com/fileadmin/user_upload/8-PDF-Docs/MagneticResonance/EPR_brochures/EPR_accessories.pdf` 26

[Car09] M. E. Carlotti, E. Ugazio, S. Sapino, I. Fenoglio, G. Greco, B. Fubini. *Role of particle coating in controlling skin damage photoinduced by titania nanoparticles.* Free Radical Research Volume 43(3): p. 312 (2009), DOI: 10.1080/10715760802716633 42

[Dea80] G. B. Deacon, R. J. Phillips. *Relationships between the Carbon-Oxygen Stretching Frequencies of Carboxylato Complexes and the Type of Carboxylate Coordination.* Coordination Chemistry Reviews Volume 33(3): p. 227 (1980), DOI: Doi 10.1016/S0010-8545(00)80455-5 9

[Dor12] D. Dorniani, M. Z. B. Hussein, A. U. Kura, S. Fakurazi, A. H. Shaari, Z. Ahmad. *Preparation of Fe_3O_4 magnetic nanoparticles coated with gallic acid for drug delivery.* International Journal of Nanomedicine Volume 7: p. 5745 (2012), DOI: 10.2147/IJN.S35746 3

[Du09] X. Du, C. Wang, M. Chen, Y. Jiao, J. Wang. *Electrochemical Performances of Nanoparticle Fe_3O_4 / Activated Carbon Supercapacitor Using KOH Electrolyte Solution.* The Journal of Physical Chemistry C Volume 113(6): p. 2643 (2009), DOI: 10.1021/jp8088269 3

[Eat10] G. R. Eaton, S. S. Eaton, D. P. Barr, R. T. Weber. *Quantitative EPR*. Springer Publishing Vienna (2010) 13, 23, 24, 25

[Els14] A. Elsukova. *Phase segregation in Fe-Cu(Ag) and diffusion enchancement in FePt-Cu gas-phase nanoparticles prepared by DC magnetron sputtering*. PhD thesis, University Duisburg-Essen (2014) 29

[Ern82] L. Ernster, K. Nordenbrand, S. Orrenius. In K. Yagi, , *Lipid Peroxides in Biology and Medicine*, Chapter Microsomal Lipid Peroxidation, p. 55 – 79. Academic Press (1982), DOI: http://dx.doi.org/10.1016/B978-0-12-768050-7.50009-3 11

[Far16] M. Farle. *private communication* (2016) 45, 55

[Feg16] T. Feggeler. *Mikromagnetische Simulationen zur statischen und dynamischen Charakterisierung von Nanopartikeln*. Masterthesis, University Duisburg-Essen (2016) 56

[Fra07] A. C. Francis, J. S. Richard. *Advanced Organic Chemistry; Part A: Structure and Mechanisms*. Springer Publishing US, 5 Edition (2007), DOI: 10.1007/978-0-387-44899-2 7

[Gil04] T. Gilbert. *A phenomenological theory of damping in ferromagnetic materials*. Magnetics, IEEE Transactions on Volume 40(6): p. 3443 (2004), DOI: 10.1109/TMAG.2004.836740 16

[Gri99] D. L. Griscom, V. Beltrán-López, C. I. Merzbacher, E. Bolden. *Electron spin resonance of 65-million-year-old glasses and rocks from the Cretaceous-Tertiary boundary*. Journal of Non-Crystalline Solids Volume 253(1-3): p. 1 (1999), DOI: http://dx.doi.org/10.1016/S0022-3093(99)00340-3 52

[Gun96] F. Gunstone. *Fatty Acid and Lipid Chemistry*. A Chapman & Hall food science book. Springer Publishing (1996) 10

[Hub98] A. Hubert, R. Schaefer. *Magnetic Domains*. Springer Publishing Berlin-Heidelberg (1998) 20

[Jam04] M. Jamet, W. Wernsdorfer, C. Thirion, V. Dupuis, P. Mélinon, A. Pérez, D. Mailly. *Magnetic anisotropy in single clusters*. Physical Review. B Volume 69: p. 024401 (2004), DOI: 10.1103/PhysRevB.69.024401 21

[Kat99] G. Kataby, M. Cojocaru, R. Prozorov, A. Gedanken. *Coating Carboxylic Acids on Amorphous Iron Nanoparticles*. Langmuir Volume 15(5): p. 1703 (1999), DOI: 10.1021/la981001w 41

[Kil] R. Kilaas. *MacTempas User Manual*. URL `http://www.emal.engin.umich.edu/pdf/MacTempasManual.pdf` 30

[Kim07] D. Kim, J. Park, K. An, N. K. Yang, J. G. Park, T. Hyeon. *Synthesis of hollow iron nanoframes*. Journal of the American Chemical Society Volume 129(18): p. 5812 (2007), DOI: 10.1021/ja070667m 3, 8, 31

[Kim09] D. Kim, N. Lee, M. Park, B. H. Kim, K. An, T. Hyeon. *Synthesis of uniform ferrimagnetic magnetite nanocubes*. Journal of the American Chemical Society Volume 131(2): p. 454 (2009), DOI: 10.1021/ja8086906 34

[Kit05] C. Kittel. *Introduction to solid state physics*. Wiley (2005) 19

[Kod99] R. Kodama. *Magnetic nanoparticles*. Journal of Magnetism and Magnetic Materials Volume 200(1-3): p. 359 (1999), DOI: http://dx.doi.org/10.1016/S0304-8853(99)00347-9 3

[Kum06] C. P. Kumar, N. O. Gopal, T. C. Wang, M. S. Wong, S. C. Ke. *EPR investigation of TiO_2 nanoparticles with temperature-dependent properties*. Journal of Physical Chemistry B Volume 110(11): p. 5223 (2006), DOI: 10.1021/jp057053t 43

[Lan35] L. D. Landau, E. Lifshitz. *On the theory of the dispersion of magnetic permeability in ferromagnetic bodies*. Phys. Z. Sowjetunion Volume 8(153): p. 101 (1935) 15

[Lee15] N. Lee, D. Yoo, D. Ling, M. H. Cho, T. Hyeon, J. Cheon. *Iron Oxide Based Nanoparticles for Multimodal Imaging and Magnetoresponsive Therapy*. Chemical Reviews Volume 115(19): p. 10637 (2015), DOI: 10.1021/acs.chemrev.5b00112 3

[Lin13] S. Lin, C. Shen, D. Lu, C. Wang, H.-J. Gao. *Synthesis of Pt nanoparticles anchored on graphene-encapsulated Fe_3O_4 magnetic nanospheres and their use as catalysts for methanol oxidation*. Carbon Volume 53: p. 112 (2013), DOI: http://dx.doi.org/10.1016/j.carbon.2012.10.037 3

[Lüt10] H. Lüth. *Solid Surfaces, Interfaces and Thin Films*. Springer Publishing Berlin-Heidelberg, 5 Edition (2010), DOI: 10.1007/978-3-642-13592-7 28

[Mah13] M. Mahdavi, M. B. Ahmad, M. J. Haron, F. Namvar, B. Nadi, M. A. Rahman, J. Amin. *Synthesis, Surface Modification and Characterisation of Biocompatible Magnetic Iron Oxide Nanoparticles for Biomedical Applications*. Molecules Volume 18(7): p. 7533 (2013), DOI: 10.3390/molecules18077533 . . 3

[Mar16a] T. Marzi. *Unknown.* PhD thesis, University Duisburg-Essen (2016). To be published 41, 45

[Mar16b] T. Marzi, S. Masur, R. Meckenstock, M. Farle. *Spin Current Detection via ESR/FMR Superposition* (2016). To be published 3, 45

[Mas16] S. Masur, B. Zingsem, T. Marzi, S. Liébana-Viñas, L. Zi-An, R. Meckenstock, M. Farle. *Characterization of the Oleic Acid/Iron Oxide Nanoparticle Interface by Magnetic Resonance* (2016). To be published 33, 49

[Mec97] R. Meckenstock. *Untersuchung der magnetischen Eigneschaften von Fe/Ag-Schichtsystemen mit der konventionellen und der ortsaufgelösten ferromagnetischen Resonanz.* PhD thesis, Ruhr-University Bochum (1997) 17

[Moo64] T. W. Moore, D. S. Rodbell. *Ferromagnetic Resonance of Single-Crystal Gadolinium.* Journal of Applied Physics Volume 35(3): p. 906 (1964), DOI: http://dx.doi.org/10.1063/1.1713530 4

[MuM] MuMax3 URL `http://mumax.github.io/` 56

[Nak08a] K. Nakamoto. *Infrared and Raman Spectra of Inorganic and Coordination Compounds Part B*, p. 1–273. John Wiley & Sons, Inc. (2008), DOI: 10.1002/9780470405888 . . . . 27, 41

[Nak08b] K. Nakamoto. *Theory of Normal Vibrations*, p. 1–147. John Wiley & Sons, Inc. (2008), DOI: 10.1002/9780470405840.ch1 41

[Née54] L. Néel. *The approaches to saturation of the magnetostriciton.* J. Phys. Radium Volume 15(5): p. 376 (1954) 21

[Nis] Nist. *Database.* URL `http://golatex.de/internetquellen-mit-bibtex-t4858.html` 40, 41

[Ohs78] T. Ohsaka, F. Izumi, Y. Fujiki. *Raman spectrum of anatase, TiO2.* Journal of Raman Spectroscopy Volume 7(6): p. 321 (1978), DOI: 10.1002/jrs.1250070606 36

[Owe05] F. J. Owens. *Ferromagnetism above room temperature in bulk sintered gallium phosphide doped with manganese.* Journal of Physics and Chemistry of Solids Volume 66(5): p. 793 (2005), DOI: 10.1016/j.jpcs.2004.10.005 . . . . 49, 51

[Pan03] Q. A. Pankhurst, J. Connolly, S. K. Jones, J. Dobson. *Applications of magnetic nanoparticles in biomedicine.* Journal of Physics D: Applied Physics Volume 36(13): p. 167 (2003) 3

[Pat08] D. Patel, J. Y. Moon, Y. Chang, T. J. Kim, G. H. Lee. *Poly(d,l-lactide-co-glycolide) coated superparamagnetic iron oxide nanoparticles: Synthesis, characterization and in vivo study as MRI contrast agent.* Colloids and Surfaces A: Physicochemical and Engineering Aspects Volume 313-314: p. 91 (2008), DOI: http://dx.doi.org/10.1016/j.colsurfa.2007.04.078 3

[Pol49] D. Polder. *On the theory of ferromagnetic resonance.* The London, Edinburgh, and Dublin Philosophical Magazine and Journal of Science Volume 40(300): p. 99 (1949), DOI: 10.1080/14786444908561215 16

[Poo97] C. P. Poole. *Electron Spin Resonance: A Comprehensive Treatise on Experimental Techniques.* Dover Publications Inc., 2 Edition (1997) 25

[Rak04] B. Rakvin, D. Žilić, N. Dalal, J. North, P. Cevc, D. Arčon, K. Zadro. *An EPR method for probing surface magnetic fields, dipolar distances, and magnetization fluctuations in single molecule magnets.* Spectrochimica Acta - Part A: Molecular and Biomolecular Spectroscopy Volume 60(6): p. 1241 (2004), DOI: 10.1016/j.saa.2003.10.022 . . . . 4, 49

[Rie13] A. Riedinger, P. Guardia, A. Curcio, M. A. Garcia, R. Cingolani, L. Manna, T. Pellegrino. *Subnanometer Local Temperature Probing and Remotely Controlled Drug Release Based on Azo-Functionalized Iron Oxide Nanoparticles.* Nano Letters Volume 13(6): p. 2399 (2013), DOI: 10.1021/nl400188q . 4

[Roo07] P. Roonasi. *Adsorption and surface reaction properties of synthesized magnetite nano-particles.* PhD thesis, LuleåUniversity of Technology (2007). URL `http://epubl.ltu.se/1402-1757/2007/67/index-en.html` 41, 42

[Say00] R. M. Sayre, J. C. Dowdy. *Titanium dioxide and zinc oxide induce photooxidation of unsaturated lipids.* Cosmetics and toiletries Volume 115(10): p. 75 (2000) 44

[Sch81] S. Schultz, E. M. Gullikson, D. R. Fredkin, M. Tovar. *Simultaneous ESR and magnetization measurements characterizing the spin glass state.* Journal of Applied Physics Volume 52(3): p. 1776 (1981), DOI: http://dx.doi.org/10.1063/1.329711 4

[Sha07] A. Shavel, B. Rodríguez-González, M. Spasova, M. Farle, Liz-Marzán. *Synthesis and Characterization of Iron/Iron Oxide Core/Shell Nanocubes.* Advanced Functional Materials Volume 17(18): p. 3870 (2007), DOI: 10.1002/adfm.200700494 . . . . 32, 33

[Sim07] K. Simeonidis, S. Mourdikoudis, M. Moulla, I. Tsiaoussis, C. Martinez-Boubeta, M. Angelakeris, C. Dendrinou-Samara,

O. Kalogirou. *Controlled synthesis and phase characterization of Fe-based nanoparticles obtained by thermal decomposition.* Journal of Magnetism and Magnetic Materials Volume 316(2): p. e1 (2007), DOI: 10.1016/j.jmmm.2007.02.009 34

[Spa02] M. Spasova, U. Wiedwald, R. Ramchal, M. Farle, M. Hilgendorff, M. Giersig. *Magnetic properties of arrays of interacting Co nanocrystals.* Journal of Magnetism and Magnetic Materials Volume 240(1 - 3): p. 40 (2002), DOI: http://dx.doi.org/10.1016/S0304-8853(01)00723-5 19

[Str01] E. Strable, J. W. M. Bulte, B. Moskowitz, K. Vivekanandan, M. Allen, , T. Douglas. *Synthesis and Characterization of Soluble Iron Oxide-Dendrimer Composites.* Chemistry of Materials Volume 13(6): p. 2201 (2001), DOI: 10.1021/cm010125i 34

[Sun04] S. Sun, H. Zeng, D. B. Robinson, S. Raoux, P. M. Rice, S. X. Wang, G. Li. *Monodisperse MFe_2O_4 (M = Fe, Co, Mn) nanoparticles.* Journal of the American Chemical Society Volume 126(1): p. 273 (2004), DOI: 10.1021/ja0380852 34

[Ter15] A. Terwey, R. Meckenstock, B. Zingsem, S. Masur, C. Derricks, F. M. Roemer, M. Farle. *Magnetic anisotropy and relaxation of single Fe/Fe_xO_y core/shell- nanocubes: a ferromagnetic resonance investigation.* submittet in AIP Advances (2015) 39

[Tho00] A. Thomas. *Fats and Fatty Oils.* Wiley-VCH Publishing (2000), DOI: 10.1002/14356007.a10_173 . . . . 7, 11

[Tru08] A. V. Trunova, R. Meckenstock, I. Barsukov, C. Hassel, O. Margeat, M. Spasova, J. Lindner, M. Farle. *Magnetic characterization of iron nanocubes.* Journal of Applied Physics Volume 104(9): p. 093904 (2008), DOI: 10.1063/1.3005985 . . . . 33, 39, 53

[Ž04] I. Žutić, J. Fabian, S. Das Sarma. *Spintronics: Fundamentals and applications.* Review of Modern Physics Volume 76: p. 323 (2004), DOI: 10.1103/RevModPhys.76.323 3

[vdL98] G. van der Laan. *Microscopic origin of magnetocrystalline anisotropy in transition metal thin films.* Journal of Physics: Condensed Matter Volume 10(14): p. 3239 (1998), URL `http://stacks.iop.org/0953-8984/10/i=14/a=012` 20

[Vo09] D. Q. Vo, E. J. Kim, S. Kim. *Surface modification of hydrophobic nanocrystals using short-chain carboxylic acids.* Journal of Colloid and Interface Science Volume 337(1): p. 75 (2009), DOI: 10.1016/j.jcis.2009.04.078 8

[Von66] S. V. Vonsovskii. *Ferromagnetic Resonance.* Pergamon (1966), DOI: http://dx.doi.org/10.1016/B978-0-08-011027-1.50005-7 .... 13, 15, 16, 20

[Wei07] J. A. Weil, J. R. Bolton. *Electron Paramagnetic Resonance: Elementary Theory and Practical Applications.* Wiley, 2nd Edition (2007) 13, 23

[Wil00] F. Wilhelm, P. Poulopoulos, P. Srivastava, H. Wende, M. Farle, K. Baberschke, M. Angelakeris, N. K. Flevaris, W. Grange, J.-P. Kappler, G. Ghiringhelli, N. B. Brookes. *Magnetic anisotropy energy and the anisotropy of the orbital moment of Ni in Ni/Pt multilayers.* Physical Review B Volume 61: p. 8647 (2000), DOI: 10.1103/PhysRevB.61.8647 20

[Wil05] N. J. Willis, A. L.ăand Turro, S. O'Brien. *Spectroscopic Characterization of the Surface of Iron Oxide Nanocrystals.* Chemistry of Materials Volume 17(24): p. 5970 (2005), DOI: 10.1021/cm051370v 47

[Win12] M. Winterer, A. Lorke, R. Schmechel, C. Schulz. *Nanoparticles from the Gas Phase: Formation, Structure, Properties.* Springer Publishing (2012), DOI: 10.1007/978-3-642-28546-2 .... 35, 36

[Wu08] W. Wu, Q. He, C. Jiang. *Magnetic Iron Oxide Nanoparticles: Synthesis and Surface Functionalization Strategies.* Nanoscale Research Letters Volume 3(11): p. 397 (2008), DOI: 10.1007/s11671-008-9174-9 8

[Yin05] Y. Yin, A. P. Alivisatos. *Colloidal nanocrystal synthesis and the organic-inorganic interface.* Nature Volume 437(7059): p. 664 (2005), DOI: 10.1038/nature04165 9

[Zha06] L. Zhang, R. He, H. C. Gu. *Oleic acid coating on the monodisperse magnetite nanoparticles.* Applied Surface Science Volume 253(5): p. 2611 (2006), DOI: 10.1016/j.apsusc.2006.05.023 41

List of publications

S. Masur, B. Zingsem, T. Marzi, S. Liébana-Viñas, Zi-An Li and R. Meckenstock, M. Farle; ***"Characterization of the Oleic Acid/Iron Oxide Nanoparticle Interface by Magnetic Resonance"***; accepted for publication in JMMM (2016)

B. Zingsem, S. Masur, P. Wendtland, M. Winklhofer, R. Salikov, F. M. Roemer, R. Meckenstock, M. Farle; ***"Specific Heat of Low Energy Spin Exitations at Elevated Temperature Measured by Ferromagnetic Resonance"***; submitted to IEEE (2016)

A. Terwey, R. Meckenstock, B. Zingsem, S. Masur, C. Derricks, F. M. Roemer, M. Farle; ***"Magnetic anisotropy and relaxation of single Fe/FexOy core/shell-nanocubes: a ferromagnetic resonance investigation"***; accepted for publication in AIP Advances (May 2016)

Acknowledgement

I would like to thank my supervisor Prof. Dr. Michael Farle for accepting me into the research group, ’Structure and Magnetism of nanoscale systems’ at the University Duisburg-Essen. Thank you for your support and your advice during this time and for giving me the opportunity to develop as a scientist.

I am grateful to Dr. Ralf Meckenstock who has so patiently taught me the magic of magnetism and ferromagnetic resonance and who has been my greatest mentor as well as friend during the course of my study. Thank you for all the fun in the lab and all the delicious ice cream. I am indebted to Dr. Florian Römer and M.Sc. Thomas Marzi who both instructed me in ultra-high vacuum techniques, and helped me with all my problems. Furthermore I must also thank B.Sc. Benjamin Zingsem, who has patiently thought me Mathematica and with whom I spend many days in the lab measuring and trying to change the world. My gratitude also goes to Dr. Detlef Spoddig and Prof. Dr. Michael Winklhofer for all the technical support and for proofreading my thesis. I thank Dr. Sara Liébana-Viñas for sharing her expertise and experience in nanoparticle synthesis and for all the support and fun during my thesis. I would also like to thank Dr. Marina Spasova for all her help with the sample characterization.

Last but not least, I would like to thank all my friends and colleagues of the research group for all the laughs and the wonderful times we have shared together. My special thanks go to the team assistance who were always there to help me during my time in the work group.

Versicherung an Eides Statt

Ich versichere an Eides statt durch meine untenstehende Unterschrift,

- dass ich die vorliegende Arbeit - mit Ausnahme der Anleitung durch die Betreuer - selbstständig und ohne fremde Hilfe durchgeführt habe und
- dass ich alle Stellen, die wörtlich oder annähernd wörtlich aus fremden Quellen entnommen sind, entsprechend als Zitate gekennzeichnet habe und
- dass ich ausschliesslich die angegebenen Quellen (Literatur, Internetseiten, sonstige Hilfsmittel) verwendet habe und
- dass ich alle entsprechenden Angaben nach besten Wissen und Gewissen vorgenommen habe,
- dass sie der Wahrheit entsprechen und dass ich nichts verschwiegen habe.

Mir ist bekannt, dass eine falsche Versicherung an Eides Statt nach §156 und nach §163 Abs. 1. des Strafgesetzbuches mit Freiheitsstrafe oder Geldstrafe bestraft wird.

Duisburg, den